Store-operated Ca^{2+} entry regulatory factor (SARAF) alters murine metabolic state age-dependent via hypothalamic pathways.

Diana Gataulin[1], Yael Kuperman[2], Michael Tsoory[2], Inbal E. Biton[2], Izhar Karbat[1], Anna Meshcheriakova[1], and Eitan Reuveny[1*]

[1]Department of Biomolecular Sciences and [2]Department of Veterinary Resources, Weizmann Institute of Science, Rehovot 760001, Israel.

[*]Corresponding author: e.reuveny@weizmann.ac.il

Highlights

- Loss/absence of SARAF facilitates age-dependent obesity with decreased metabolic rate, lean mass, and locomotion, without affecting food consumption.
- Loss of SARAF leads to lipid droplet hypertrophy, BAT whitening and age-dependent hepatic steatosis.
- Mice lacking SARAF expression in the PVN have an increased metabolic rate, decreased BAT whitening, and are protected from sarcopenic obesity.
- SARAF ablation in hepatocytes increases SOCE, elevates Ca^{2+} oscillation in response to vasopressin, and increases the mitochondria's spare respiratory capacity.
- Loss of SARAF leads to decreased hippocampal proliferation, sensitized HPA-axis and changes in anxiety-related behavior.

Summary

Store-operated Ca2+ entry (SOCE) is a vital process aimed at refilling cellular internal Ca^{2+} stores, and a primary cellular-signaling driver of transcription factors entry to the nucleus. SARAF (SOCE associated regulatory factor)/TMEM66 is an endoplasmic reticulum (ER) resident transmembrane protein that promotes SOCE inactivation and prevents Ca^{2+} overfilling of the cell. Here we demonstrate that mice deficient in SARAF develop age-dependent sarcopenic obesity with decreased energy expenditure, lean mass and locomotion without affecting food consumption. Moreover, SARAF ablation reduces hippocampal proliferation, modulates the activity of the hypothalamus-pituitary-adrenal (HPA) axis, and mediates changes in anxiety-related behaviors. Interestingly, selective SARAF ablation in the paraventricular nucleus (PVN) of the hypothalamus protects from old age-induced obesity and preserves locomotion, lean mass and energy expenditure, suggesting an opposing, site-specific role for SARAF. Lastly, SARAF ablation in hepatocytes leads to elevated SOCE, elevated vasopressin-induced Ca^{2+} oscillations, and an increased mitochondrial spare respiratory capacity, thus providing insights into the cellular mechanisms that may affect the global phenotypes. These effects may be mediated via the liver X

40 receptor (LXR) and IL-1 signaling metabolic regulators explicitly altered in SARAF ablated cells.
41 In short, our work supports both central and peripheral roles of SARAF in regulating metabolic,
42 behavioral, and cellular responses.

43

44

45 **Introduction**

46 Overweight and obesity affects almost 2 billion people worldwide (as calculated by World Health
47 Organization-WHO in 2016) and is considered a 21st-century pandemic. Diet and exercise are
48 considered the primary prevention and treatment strategies (https://www.who.int/health-
49 topics/obesity#tab=tab_1). However, understanding the genetic factors involved in the central
50 circuitry, metabolism, and adipose tissue homeostasis may improve the ability to treat obesity with
51 precision (González-Muniesa et al., 2017; Van Der Klaauw and Farooqi, 2015). Metabolic
52 homeostasis of the entire organism is a balanced feedback mechanism involving both the CNS and
53 periphery, where the hypothalamic paraventricular nucleus (PVN) plays a central role (Kim et al.,
54 2018) ;it directly and indirectly regulates critical hormones as corticosterone (cortisol in humans),
55 adrenaline, vasopressin, oxytocin, thyrotropin-releasing hormone (TRH) (Herman et al., 2016). Of
56 which regulate the body's metabolic state (Qin et al., 2018a). Many intracellular pathways respond
57 to these signaling cues to affect metabolic homeostasis, where changes in intracellular Ca^{2+} levels
58 are central (Berridge, 2016; Clapham, 2007; Pozzan et al., 1994). It is thus critical to have tight
59 regulation of intracellular and intraorganelle Ca^{2+} levels. This task is a well-coordinated action by
60 many proteins that either pump Ca^{2+} from the cytosol or into intracellular organelles such as
61 mitochondria and the endoplasmic reticulum (ER) (Pozzan et al., 1994).

62 Store-operated calcium entry (SOCE) is one of several processes that participate in the cell's Ca^{2+}
63 homeostasis (Prakriya and Lewis, 2015) . In most cell types, it replenishes the Ca^{2+} cellular stores,
64 like the ER and mitochondria, and in some it also plays a crucial role in transcription factor's entry
65 to the nucleus to activate gene transcription (Hogan et al., 2010). SOCE is activated following the
66 release of Ca^{2+} from ER stores by inositol tri-phosphate (IP_3), the product of the breakdown of
67 phosphatidylinositol diphosphate (PIP2) by PLCβ or PLCγ activation via G_q/11-coupled G-
68 protein-linked receptors, or receptor tyrosine kinases, respectively (Berridge, 1993; Putney, 1986).
69 Two essential components are required for SOCE activity, stromal interaction molecule (STIM),
70 an ER transmembrane protein with a Ca^{2+} sensing domain at its ER luminal side, and a plasma
71 membrane (PM) resident Ca^{2+} channel, (Orai) (Feske et al., 2006; Liou et al., 2005; Prakriya et al.,
72 2006; Roos et al., 2005; Yeromin et al., 2006). SOCE is activated following the depletion of Ca^{2+}
73 from the ER lumen, oligomerization of STIM, and activation of Orai at PM-ER junctions to allow
74 the flow of Ca^{2+} ions into the cell, to replenish the depleted stores. An additional layer of SOCE

activity is provided by the interactions of STIM and Orai with the transient receptor potential channels (TRPCs), non-selective cation channels (Ambudkar et al., 2016; Liao et al., 2007).

Calcium signaling involving the ER and mitochondria is compromised in obesity and metabolic diseases (Arruda and Hotamisligil, 2015; Berridge, 2016). SOCE is a crucial element in lipid metabolism and adiposity; specifically, it plays a role in the mobilization of fatty acids from lipid droplets, lipolysis, and mitochondrial fatty acid oxidation (Baumbach et al., 2014; Cuk et al., 2017). Additionally, SOCE is necessary for glucose-stimulated pancreatic insulin secretion (Sabourin et al., 2015; Tamarina et al., 2005). Moreover, Ca^{2+} signaling and SOCE are involved in proper liver function, including bile secretion, proliferation, oscillatory response to hormones, cholesterol, and glucose metabolism (Amaya and Nathanson, 2013; Aromataris et al., 2008). Alterations in liver SOCE result in decreased ER Ca^{2+} content, ER stress, inflammation, impaired insulin function, and abnormal glucose metabolism (Arruda et al., 2014; Wilson et al., 2015). Furthermore, SOCE was found to be impaired in the liver of obese murine models (Arruda et al., 2017; Park et al., 2010). SOCE was also implicated in myocytes' function, specifically its importance in the proper function of the sarcoplasmic reticulum (Stiber et al., 2008; Wei-Lapierre et al., 2013; Zhao et al., 2015). Furthermore, SOCE function in myocytes distinguishes between aged and young muscle (Thornton et al., 2011; Zhao et al., 2008).

SARAF is an ER resident protein that we previously reported to associate with STIM and promote SOCE inactivation (Palty et al., 2012). SARAF plays a key role in shaping cytosolic Ca^{2+} signals and determining the content of the major intracellular Ca^{2+} stores, a role that is probably important in protecting the cell from Ca^{2+} overfilling. SARAF is localized to PIP2-rich PM junctions (Cao et al., 2015) and is activated by dimerization at its luminal end (Kimberlin et al., 2019) when stores are full, by a still unknown mechanism. Reduced SARAF levels increase intracellular SOCE and was recently found to be involved in several pathological conditions such as pancreatitis and cerebral ischemia (La Russa et al., 2020; Son et al., 2019). Moreover, SARAF is an androgen-responsive marker for prostate cancer and it regulates mTOR-dependent cardiac growth (Romanuik et al., 2009; Sanlialp et al., 2020). Here we report on the consequences of knocking out SARAF, both globally and in PVN-specific manner in mice. KO of SARAF introduces a new role for SARAF in physiological context. SARAF KO mice gain weight and loose lean mass at a later age. This weight gain is not the consequence of increased food intake but dependent on PVN-

105 associated circuits. At the cellular level, SARAF increases mitochondrial respiration in addition to
106 its expected reduction of SOCE activity. This report may place SARAF as an important component
107 in the pathophysiology of obesity.

108

109

Results and Discussion

Generation of SARAF-KO mice. To study its physiological role, we used the knock-out mouse project (KOMP) repository, first to create SARAF LacZ knock-in cassette inserted mice and then SARAF loxP-floxed conditional mice, termed $SARAF^{fl/fl}$, as described in the experimental procedures section and graphical representation (Figure 1A). SARAF was previously shown to be highly expressed in the immune and neuronal tissues (Palty et al., 2012); we focused on its expression in the brain via LacZ staining and found it has a marked expression in the hippocampus, hypothalamus (specifically the PVN) and the amygdala (Figure 1B). Later, by crossing the conditional $SARAF^{fl/fl}$ mice to the ubiquitously expressing PGK promoter-driven Cre recombinase mice to generate PGK-Cre^{+}:$SARAF^{fl/fl}$, whole - body knock-out mice, termed SARAF-KO. The knockout of SARAF was validated via Western blotting of the brain tissue and compared with their littermates $SARAF^{fl/fl}$PGK-Cre^{-}, who were homozygous to the floxed SARAF, but did not express Cre recombinase, termed SARAF-WT (Supp. 1A). SARAF knock-out mice were viable and bred normally with Mendelian distribution.

SARAF-KO mice have impaired metabolic function and lipid accumulation. Male SARAF-KO mice were compared with their WT littermates and were found to have a significant increase in body weight. The weight differences were significantly higher from early adulthood (three months), where the KO mice weighted on average about 10% more than the WT mice. The weight differences increased with age. At 1 year old KO mice weighted nearly 20% more than the WT mice (Figure 1C). Linear growth was not altered in the SARAF-KO mice (Supp.1B). Interestingly, the weight differences were also reflected in body composition alterations, including an increased percentage of fat mass and lower percentage of lean mass in the KO mice, suggesting a possible role for SARAF in mediating sarcopenic obesity-like symptoms (Figure 1D). Indirect calorimetry assessment of SARAF-KO mice revealed a lower metabolic rate (as manifested in heat production) and reduced locomotion (measured during the active phase in the diurnal cycle) (Figure 1E-F). The abovementioned changes were not associated with significant differences in food intake (Supp.1C). Moreover, food intake after five hours fasting in a refeed experiment did not alter either the weight loss or the weight gain following the experiment (Supp.1D). Interestingly, despite the altered body weight and the body composition, the mice were not diabetic or pre-diabetic since

139 they present with a normal fasting glucose level and had a normal response to a glucose load (as
140 assessed by glucose tolerance test (GTT)) (Figure 1G).

141 We then examined the adipose tissue distribution in the elderly SARAF-KO mice using computed
142 tomography (CT) imaging and found that the excess fat was distributed throughout the body with
143 a high tendency for abdominal accumulation (Figure 2A-C). Hematoxylin and eosin (H&E) stained
144 white adipose tissue (WAT) droplets size analysis of inguinal and visceral adipose tissues (iWAT
145 and vWAT, respectively), revealed significant hypertrophy of fat cells. Moreover, we found that
146 fat was accumulated both in the intracapsular brown adipose tissue (iBAT) and in the liver,
147 resulting in iBAT whitening and hepatic steatosis (Figure 2D-H). These histological phenotypes
148 were seen in 3-month-old mice and upsurge in 1-year-old mice, except liver fat accumulation,
149 which is not obvious yet in younger mice (Supp.1E-I). BAT is an organ that contributes to systemic
150 metabolic homeostasis and thermoregulation, and its size is associated with various pathologic
151 conditions including obesity (Enerbäck, 2010; Shimizu and Walsh, 2015). Interestingly, iBAT
152 whitening can be prevented by inhibiting Ca^{2+} overload in the mitochondria, (Gao et al., 2020).
153 Moreover, the hepatic steatosis is accompanied by cellular Ca^{2+} imbalance and is a predisposition
154 for a non-alcoholic fatty liver disease that might lead to liver cirrhosis and cancer (Ali et al., 2017).
155 The weigh- and fat-associated changes in elderly SARAF ablated mice were also accompanied by
156 subclinical hypothyroidism, manifested by normal serum thyroxine and cholesterol, and elevated
157 TSH levels (Fatourechi, 2009)(Figure 2I-K). Subclinical elevation of TSH might influence resting
158 metabolic rate and may hint at early thyroid dysfunction (Tagliaferri et al., 2001). The correlation
159 between the old age increase in TSH and hepatic steatosis may raise the possibility of a thyroid-
160 liver interaction (Huang et al., 2013).

161

162 **SARAF ablation in SIM1 neurons improves metabolic function and hints toward**
163 **hypothalamic metabolic feedback.** SARAF regulated metabolic phenotypes discussed above
164 could stem from any several metabolic organs, including adipose, muscle and brain derived
165 regulation. Because of the marked SARAF expression in the hypothalamus, we chose to focus on
166 the role of hypothalamic SARAF in energy homeostasis. To this end, we crossed the $SARAF^{fl/fl}$
167 mice to SIM1 promoter-driven Cre-recombinase expressing mice (SIM1-Cre) (Balthasar et al.,

168 2005) to induce SARAF deletion specifically in the hypothalamic PVN neurons, termed SARAF-
169 SIM1KO. Mice were validated via site-specific punch-PCR of the PVN (Suppl. 2A). Unlike
170 SARAF-KO, three month old SARAF-SIM1KO mice had similar body weights and composition
171 to their WT littermates. However, at the age of one year old, these mice were found to have
172 improved age-related metabolic phenotypes, inversely mirroring the whole body SARAF-KO. At
173 1 year old, SARAF-SIM1KO mice had lower body weight with a reduced percentage of fat mass
174 and an increased percentage of lean mass than SARAF-SIM1WT littermates (Figure 3A-B). Like
175 the whole body knocked-out mice, SARAF-SIM1KO mice did not have an altered response to
176 glucose, or differences in food consumption either under basal or refeed challenged conditions
177 (Figure 3C and Supp. 2B-C). Moreover, their heat production and locomotor activity were elevated
178 in the opposite tendency to the SARAF-KO mice (Figure 3D-F). Those phenotypes are clear only
179 at old age (over 1-years-old) except for increased locomotion, which was already evident in 3-
180 month-old mice (Supp.2D-2F). The increased locomotion in SARAF-SIM1KO mice is of interest
181 since it is consistent from a young age to old age and thus may drive the phenotype by increasing
182 lean mass and/or by changing energy expenditure. Several studies have implicated hypothalamic
183 PVN in the regulation of locomotion (Gladfelter and Brobeck, 1962; McCormick and Njeri
184 Ibrahim, 2006; Mönnikes et al., 1992). Interestingly, when examining lipid accumulation in the
185 SARAF-SIM1KO mice, we noticed that BAT had reduced fat accumulation compared with the
186 wild type littermates. We did not witness differences in WAT droplet size or fat accumulation in
187 the liver (Figure 3G-K). When challenging these mice with diet rich in fat and carbohydrates food
188 (Western diet) for 18 weeks, their total increases in body weight, composition and calorimetry
189 analysis, were similar between the two groups (Supp.3A-E). In Western diet fed mice lipid
190 accumulation phenotype, glucose tolerance, and refeed responses were unchanged as well (Supp.
191 3E-J), thus strengthening the assumption that SARAF related metabolic phenotypes in SARAF
192 SIM1KO mice are not related to food intake related mechanism. These results point toward the
193 coordination of BAT and thermogenesis by the PVN via the Ca^{2+} homeostasis mechanism (Qin et
194 al., 2018b). It is of note that SARAF SIM1KO mice did not exhibit altered anxiety-related
195 behavioral phenotype suggesting that SARAF, although ubiquitously expressed, plays a site-
196 specific role (supp. 4G-I).

197

198 **SARAF ablation decreases hippocampal proliferation, affects the stress response and HPA-**
199 **axis activation.** SARAF was highly expressed in the hippocampus (Figure 1B) and specifically in
200 a subset of doublecortin (DCX) positive neuronal progenitors, indicative of proliferating neuronal
201 stem cells (Supp.4A). Since hippocampal proliferation has a marked impact on anxiety and
202 metabolism via the HPA-axis (Kanoski and Grill, 2017; Snyder et al., 2011), we sought to examine
203 the impact of SARAF on hippocampal proliferation and its effect on the hypothalamus-pituitary-
204 adrenal (HPA) axis, as, altered function of this system may affect the metabolic phenotype and
205 may account, in part, for the phenotypes reported above. EdU (5-ethynyl-2′-deoxyuridine)
206 incorporation was used to examine hippocampal cell proliferation in the SARAF-WT and in the
207 SARAF-KO mice. EDU incorporation assay revealed a significant decrease in proliferation in the
208 dorsal and the ventral hippocampus dentate gyrus in the SARAF-KO mice (Figure 4A). This
209 decrease was independently validated via an immunostaining against proliferating cell nuclear
210 antigen (PCNA) as the proliferation marker (supp. 4B) and repeated in primary mouse embryonic
211 fibroblast (MEF) cultures derived from SARAF-WT and SARAF-KO using staining for Ki67
212 expression (Supp. 4C).

213 Behaviorally, SARAF-KO mice exhibited decreased anxiety-like behavior as manifested in the
214 dark-light transfer (DLT) by increased time spent in the lit compartment (Figure 4B-C), and in the
215 acoustic startle response (ASR) experiment, where they exhibited longer reaction time in the first
216 set of stimulus presentations (Figure 4D). Counterintuitively, SARAF knocked out mice exhibited
217 a mild increase in HPA-axis activation, as suggested by a stronger immediate corticosterone
218 response to restraint-stress (Figure 4E). This discrepancy may stem from differences in the timing
219 of assessment; 5 to 10 min following the initiation of the exposure to stress in the DLT and ASR
220 tests, as opposed to about 30 min in the CORT assessment. Interestingly, despite the reduced
221 neurogenesis observed, long-term memory, assessed using the Morris water maze (Supp. 4F), and
222 short-term memory, assessed using the Y-maze (Supp. 4D-E), were not altered.

223

224 **SARAF ablation leads to increased cellular SOCE, elevated mitochondrial spare respiratory**
225 **capacity, and altered gene expression patterns.** Cellular metabolic functions influence global
226 metabolic phenotypes and behavior; specifically, mitochondrial respiration greatly influences

227 global metabolic phenotypes (Picard et al., 2015). Moreover, since the hypothalamus, directly via
228 neuronal connections and indirectly via hormonal secretion, regulate metabolic organs (Gore,
229 2013; Roh et al., 2016), we sought to examine whether the cellular metabolic functions were
230 consistent with the global phenotypes we observed in the KO animals. Specifically, the liver is
231 tightly regulated by the PVN via a direct neuronal innervation and hormonal regulation (O'Hare
232 and Zsombok, 2016; Uyama et al., 2004). For this reason, we extracted primary hepatocytes from
233 SARAF-KO mice and examined their Ca^{2+} signaling and SOCE by FURA-2AM-based Ca^{2+}
234 imaging. We induced SOCE by the transient sarco/endoplasmic reticulum Ca^{2+}-ATPase (SERCA)
235 inhibitor BHQ. SOCE activity was elevated in the knocked-out hepatocytes, confirming our
236 previous in vitro experiments (Palty et al., 2012). Hepatocyte SOCE was inhibited by the Orai
237 inhibitors La^{3+} and 2-ABP, therefore, hinting at the involvement of the classical SOCE and the
238 involvement of the STIM-Orai machinery (Bird and Putney, 2018) (Figure 4F).

239 Ca2+ oscillations are a significant driver of cellular signaling, and it are mediated by SOCE and
240 the mitochondrial Ca^{2+} uptake (Dolmetsch et al., 1998). Vasopressin is a pituitary secreted
241 hormone that regulates several physiological functions, including behavior, thermoregulation,
242 water absorption, liver function, and adipogenesis (Jones et al., 2008; Maus et al., 2017). When
243 examining Ca^{2+} oscillations triggered by physiological levels of vasopressin (1nM), we observed
244 a marked increase in release amplitude and increased oscillation intervals in the knocked-out
245 hepatocytes (Figure 4G). The latter strengthens the idea that SARAF may affect hypothalamic
246 control over metabolic organs, including the liver. Next, we sought to examine cellular metabolic
247 function by measuring mitochondrial respiration by directly examining the cellular oxygen
248 consumption rate (Traba et al., 2016). This function is highly influenced by the cellular Ca^{2+} levels
249 and influences global metabolic phenotypes (Böhm et al., 2020; Gherardi et al., 2020; Picard et
250 al., 2015). Cellular mitochondrial respiration was markedly altered in SARAF knocked out
251 hepatocytes, having a significantly higher spare respiratory capacity (SRC) function (Figure 4H).
252 These findings suggest that SARAF, via the modulation of SOCE activity, has a great influence
253 on metabolic organs at a cellular level, like the liver, with altered mitochondrial metabolism and
254 SOCE. Since Ca^{2+}, in addition to its direct regulatory action, can affect at longer time scales gene
255 transcription, we set to examine gene transcription patterns by RNA sequencing embryonic
256 fibroblast (MEF) cells derived from SARAF-WT and SARAF-KO animals. We analyzed the
257 results for canonical pathway enrichment using QIAGEN's Ingenuity® software and identified

258 that LXR (Liver X receptor)/RXR (Retinoid X receptor) signaling pathway was significantly
259 altered (Figure 4I), hinting, again, at SARAF importance in proper liver function. The LXR/RXR
260 signaling pathway genes that were altered include IL1α, IL33, LBP, and ApoD, all of which have
261 indications in metabolic function (Jakobsson et al., 2012; Miller et al., 2010). LXR/RXR and the
262 related LXR regulated IL-1-signaling pathways were previously shown to influence metabolism
263 via the hypothalamus and directly influencing adipose tissue and the liver (Barbier et al., 2019;
264 Ericsson et al., 1994; Hong and Tontonoz, 2014; Kruse et al., 2017).

265 **Conclusion**

266 This study demonstrates that SARAF is involved in the physiological regulation of age-dependent
267 metabolic rate (as manifested by energy expenditure) and locomotion, without affecting food
268 consumption or clear blood glucose handling. Moreover, SARAF was involved in a complex
269 metabolic phenotype that includes lipid metabolism regulation in the adipose tissue, the BAT and
270 liver. These global phenotypes were accompanied by SARAF-mediated cellular metabolic
271 functions, including hepatocyte's SOCE, vasopressin evoked Ca^{2+} oscillations and mitochondria's
272 spare respiratory capacity. Examining SARAF's contribution to the central nervous system
273 regulation functions, indicted its involvement in PVN regulated autonomic-sympathetic control of
274 energy expenditure, locomotion, and BAT profile. Moreover, SARAF was found to regulate
275 hippocampal proliferation, while having some effects on the HPA-axis and anxiety-related
276 behavior.

277 Cellular Ca^{2+} balance is a major factor in fine-tuning metabolic function in different organs,
278 including the liver, muscle, adipose tissues and neurons; even slight changes in Ca^{2+} levels might
279 affect their function (Ong et al., 2019; Toescu and Verkhratsky, 2007). SARAF is expressed in the
280 Sim-1 expressing neurons of the brain, the muscle and BAT. SOCE homeostasis, regulated by
281 SARAF, is especially important in a subset of specific cells/tissues, described in this study, it is
282 suggested, however, that additional subtle and yet to be discovered SARAF related physiological
283 functions are probably affected as well. Moreover, other proteins essential for maintaining Ca^{2+}
284 homeostasis, like SERCA, whose activity is reduced with aging (Lompré et al., 1991) may be more
285 essential in the absence of SARAF. In this study, the influence of SARAF on SRC was indicated
286 in the hepatocytes OCR measurements, underlining the importance of maintaining appropriate

287 Ca^{2+} levels for healthy-cell function (Chemaly et al., 2018). Interestingly, SRC is a known
288 influencer over aging muscle function, and a driver of sarcopenia (Hiona et al., 2010). Thus, SRC
289 might be the driver of SARAF involvement in lean mass maintenance. However, in the liver,
290 SARAF causes improved SRC, seemingly opposite to the previously described papers, however,
291 increase in SRC is possible, in case of damaged oxidative phosphorylation as indicated in some
292 reports (Porter et al., 2015). Interestingly, and relating to our running wheel data, training increases
293 in aged muscle (Waters et al., 2003). Furthermore, SRC is also elevated in the hyperglycemic
294 adipocytes, allowing for fast adaptation and recovery, SARAF ablation in the metabolic organ
295 forces increasing SRC levels as an adaptive response to less than favorable conditions (Keuper et
296 al., 2014).

297 SARAF role in hippocampal neurons is still in need of further refining; specifically, it is perplexing
298 that SARAF involvement in hippocampal proliferation did not alter learning and memory.
299 Nevertheless, it has been previously discussed that significant cellular aberration should occur to
300 influence a behavioral phenotype (Dauer and Przedborski, 2003), given the importance of Ca^{2+}
301 regulation for cellular physiology, it is possible that compensatory mechanisms exist to provide an
302 additional layer of protection from an aberrant Ca^{2+} steady-state levels. This can be in the factors
303 associated with SOCE, pumps that clear cytosolic Ca^{2+}, or an increase in the cell-buffering capacity
304 (Carreras-Sureda et al., 2013; Feng et al., 2006, 2010; Karakus et al.; Srivats et al., 2016).

305 Collectively, our study shows for the first time, to the best of our knowledge, that SARAF is an
306 essential contributor to the dysregulation of general and PVN regulated metabolic states.
307 Moreover, it is a novel model for age-dependent sarcopenic obesity, which is not dependent on
308 feeding or is accompanied by diabetes. Pharmacological targeting of the SARAF signaling
309 pathway may provide a novel approach for treating sarcopenic obesity.

310

311 **Acknowledgments**

312 This study was supported, in part, by the US-Israel Binational Foundation (2015298), the Minerva
313 Foundation, the Willner Family Fund and Yeda-Sela Center, all to E.R. E.R. is the incumbent of
314 the Charles H. Hollenberg Professorial Chair.

315 **References**

316 Akselrod-Ballin, A., Dafni, H., Addadi, Y., Biton, I., Avni, R., Brenner, Y., and Neeman, M.
317 (2016). Multimodal Correlative Preclinical Whole Body Imaging and Segmentation. Scientific
318 Reports *6*, 1–13. https://doi.org/10.1038/srep27940.

319 Ali, E.S., Rychkov, G.Y., and Barritt, G.J. (2017). Metabolic disorders and cancer: Hepatocyte
320 store-operated Ca2+ channels in nonalcoholic fatty liver disease. In Advances in Experimental
321 Medicine and Biology, (Springer New York LLC), pp. 595–621.

322 Amaya, M.J., and Nathanson, M.H. (2013). Calcium signaling in the liver. Compr Physiol *3*,
323 515–539. https://doi.org/10.1002/cphy.c120013.

324 Ambudkar, I.S., de Souza, L.B., and Ong, H.L. (2016). TRPC1, Orai1, and STIM1 in SOCE:
325 Friends in tight spaces. Cell Calcium https://doi.org/10.1016/j.ceca.2016.12.009.

326 Aromataris, E.C., Castro, J., Rychkov, G.Y., and Barritt, G.J. (2008). Store-operated Ca2+
327 channels and Stromal Interaction Molecule 1 (STIM1) are targets for the actions of bile acids on
328 liver cells. Biochimica et Biophysica Acta - Molecular Cell Research *1783*, 874–885.
329 https://doi.org/10.1016/j.bbamcr.2008.02.011.

330 Arruda, A.P., and Hotamisligil, G.S. (2015). Calcium homeostasis and organelle function in the
331 pathogenesis of obesity and diabetes. Cell Metabolism *22*, 381–397.
332 https://doi.org/10.1016/j.cmet.2015.06.010.

333 Arruda, A.P., Pers, B.M., Parlakgül, G., Güney, E., Inouye, K., and Hotamisligil, G.S. (2014).
334 Chronic enrichment of hepatic endoplasmic reticulum–mitochondria contact leads to
335 mitochondrial dysfunction in obesity. https://doi.org/10.1038/nm.3735.

336 Arruda, A.P., Pers, B.M., Parlakgul, G., Güney, E., Goh, T., Cagampan, E., Lee, G.Y.,
337 Goncalves, R.L., and Hotamisligil, G.S. (2017). Defective STIM-mediated store operated Ca2+
338 entry in hepatocytes leads to metabolic dysfunction in obesity. Elife *6*.
339 https://doi.org/10.7554/eLife.29968.

340 Balthasar, N., Dalgaard, L.T., Lee, C.E., Yu, J., Funahashi, H., Williams, T., Ferreira, M., Tang,
341 V., McGovern, R.A., Kenny, C.D., et al. (2005). Divergence of melanocortin pathways in the
342 control of food intake and energy expenditure. Cell *123*, 493–505.
343 https://doi.org/10.1016/j.cell.2005.08.035.

344 Bannerman, D.M., Sprengel, R., Sanderson, D.J., McHugh, S.B., Rawlins, J.N.P., Monyer, H.,
345 and Seeburg, P.H. (2014). Hippocampal synaptic plasticity, spatial memory and anxiety. Nature
346 Reviews Neuroscience *15*, 181–192. https://doi.org/10.1038/nrn3677.

347 Barbier, L., Ferhat, M., Salamé, E., Robin, A., Herbelin, A., Gombert, J.M., Silvain, C., and
348 Barbarin, A. (2019). Interleukin-1 family cytokines: Keystones in liver inflammatory diseases.
349 Frontiers in Immunology *10*. https://doi.org/10.3389/fimmu.2019.02014.

350 Baumbach, J., Hummel, P., Bickmeyer, I., Kowalczyk, K.M., Frank, M., Knorr, K., Hildebrandt,
351 A., Riedel, D., Jäckle, H., and Kühnlein, R.P. (2014). A drosophila in vivo screen identifies
352 store-operated calcium entry as a key regulator of adiposity. Cell Metabolism *19*, 331–343.
353 https://doi.org/10.1016/j.cmet.2013.12.004.

354 Berridge, M.J. (1993). Inositol trisphosphate and calcium signalling.

355 Berridge, M.J. (2016). The Inositol Trisphosphate/Calcium Signaling Pathway in Health and
356 Disease. Physiol Rev *96*, 1261–1296. https://doi.org/10.1152/physrev.00006.2016.-Many.

357 Bird, G.S., and Putney, J.W. (2018). Pharmacology of Store-Operated Calcium Entry Channels.
358 In Calcium Entry Channels in Non-Excitable Cells, (CRC Press), pp. 311–324.

359 Böhm, A., Keuper, M., Meile, T., Zdichavsky, M., Fritsche, A., Häring, H.-U., de Angelis, M.H.,
360 Staiger, H., and Franko, A. (2020). Increased mitochondrial respiration of adipocytes from
361 metabolically unhealthy obese compared to healthy obese individuals. Scientific Reports *10*,
362 12407. https://doi.org/10.1038/s41598-020-69016-9.

363 Cao, X., Choi, S., Maléth, J.J., Park, S., Ahuja, M., and Muallem, S. (2015). The ER/PM
364 microdomain, PI(4,5)P_2 and the regulation of STIM1-Orai1 channel function. Cell Calcium *58*,
365 342–348. https://doi.org/10.1016/j.ceca.2015.03.003.

366 Carreras-Sureda, A., Cantero-Recasens, G., Rubio-Moscardo, F., Kiefer, K., Peinelt, C.,
367 Niemeyer, B.A., Valverde, M.A., and Vicente, R. (2013). ORMDL3 modulates store-operated
368 calcium entry and lymphocyte activation. Human Molecular Genetics *22*, 519–530.
369 https://doi.org/10.1093/hmg/dds450.

370 Chemaly, E.R., Troncone, L., and Lebeche, D. (2018). SERCA Control of Cell Death and
371 Survival Graphical abstract. Cell Calcium *69*, 46–61. https://doi.org/10.1016/j.ceca.2017.07.001.

372 Clapham, D.E. (2007). Calcium signaling. Cell *131*, 1047–1058.
373 https://doi.org/10.1016/j.cell.2007.11.028.

374 Cuk, M., Patel, B., Moore, K.J., Cuervo, A.M., and Feske, S. (2017). Store-Operated Ca 2+
375 Entry Controls Induction of Lipolysis and the Transcriptional Reprogramming to Lipid
376 Metabolism. Cell Metabolism *25*, 698–712. https://doi.org/10.1016/j.cmet.2016.12.021.

377 Dauer, W., and Przedborski, S. (2003). Parkinson's disease: Mechanisms and models. Neuron
378 *39*, 889–909. https://doi.org/10.1016/S0896-6273(03)00568-3.

379 Dolmetsch, R.E., Xu, K., and Lewis, R.S. (1998). Calcium oscillations increase the efficiency
380 and specificity of gene expression. Nature *392*, 933–936. https://doi.org/10.1038/31960.

381 Enerbäck, S. (2010). Human Brown Adipose Tissue. Cell Metabolism *11*, 248–252.
382 https://doi.org/10.1016/j.cmet.2010.03.008.

383 Ericsson, A., Kovács, K.J., and Sawchenko, P.E. (1994). A functional anatomical analysis of
384 central pathways subserving the effects of interleukin-1 on stress-related neuroendocrine

385 neurons. Journal of Neuroscience *14*, 897–913. https://doi.org/10.1523/jneurosci.14-02-
386 00897.1994.

387 Fatourechi, V. (2009). Subclinical Hypothyroidism: An Update for Primary Care Physicians.
388 Mayo Clinic Proceedings *84*, 65–71. https://doi.org/https://doi.org/10.4065/84.1.65.

389 Feng, J.M., Hu, Y.K., Xie, L.H., Colwell, C.S., Shao, X.M., Sun, X.P., Chen, B., Tang, H., and
390 Campagnoni, A.T. (2006). Golli Protein Negatively Regulates Store Depletion-Induced Calcium
391 Influx in T Cells. Immunity *24*, 717–727. https://doi.org/10.1016/j.immuni.2006.04.007.

392 Feng, M., Grice, D.M., Faddy, H.M., Nguyen, N., Leitch, S., Wang, Y., Muend, S., Kenny, P.A.,
393 Sukumar, S., Roberts-Thomson, S.J., et al. (2010). Store-independent activation of Orai1 by
394 SPCA2 in mammary tumors. Cell *143*, 84–98. https://doi.org/10.1016/j.cell.2010.08.040.

395 Feske, S., Gwack, Y., Prakriya, M., Srikanth, S., Puppel, S.H., Tanasa, B., Hogan, P.G., Lewis,
396 R.S., Daly, M., and Rao, A. (2006). A mutation in Orai1 causes immune deficiency by
397 abrogating CRAC channel function. Nature *441*, 179–185. https://doi.org/10.1038/nature04702.

398 Gao, P., Jiang, Y., Wu, H., Sun, F., Li, Y., He, H., Wang, B., Lu, Z., Hu, Y., Wei, X., et al.
399 (2020). Inhibition of mitochondrial calcium overload by SIRT3 prevents obesity-or age-related
400 whitening of brown adipose tissue. Diabetes *69*, 165–180. https://doi.org/10.2337/db19-0526.

401 Gherardi, G., Monticelli, H., Rizzuto, R., and Mammucari, C. (2020). The Mitochondrial Ca2+
402 Uptake and the Fine-Tuning of Aerobic Metabolism. Frontiers in Physiology *11*.
403 https://doi.org/10.3389/fphys.2020.554904.

404 Gladfelter, W.E., and Brobeck, J.R. (1962). Decreased spontaneous locomotor activity in the rat
405 induced by hypothalamic lesions. Am J Physiol *203*, 811–817.
406 https://doi.org/10.1152/ajplegacy.1962.203.5.811.

407 González-Muniesa, P., Mártinez-González, M.A., Hu, F.B., Després, J.P., Matsuzawa, Y., Loos,
408 R.J.F., Moreno, L.A., Bray, G.A., and Martinez, J.A. (2017). Obesity. Nature Reviews Disease
409 Primers *3*, 1–18. https://doi.org/10.1038/nrdp.2017.34.

410 Gore, A.C. (2013). Neuroendocrine Systems. Fundamental Neuroscience 799–817.
411 https://doi.org/10.1016/B978-0-12-385870-2.00038-X.

412 Halpern, K.B., Shenhav, R., Massalha, H., Toth, B., Egozi, A., Massasa, E.E., Medgalia, C.,
413 David, E., Giladi, A., Moor, A.E., et al. (2018). Paired-cell sequencing enables spatial gene
414 expression mapping of liver endothelial cells. Nature Biotechnology *36*, 962.
415 https://doi.org/10.1038/nbt.4231.

416 Herman, J.P., McKlveen, J.M., Ghosal, S., Kopp, B., Wulsin, A., Makinson, R., Scheimann, J.,
417 and Myers, B. (2016). Regulation of the hypothalamic-pituitary- adrenocortical stress response.
418 Compr Physiol *6*, 603–621. https://doi.org/10.1002/CPHY.C150015.

419 Hiona, A., Sanz, A., Kujoth, G.C., Pamplona, R., Seo, A.Y., Hofer, T., Someya, S., Miyakawa,
420 T., Nakayama, C., Samhan-Arias, A.K., et al. (2010). Mitochondrial DNA mutations induce

421 mitochondrial dysfunction, apoptosis and sarcopenia in skeletal muscle of mitochondrial DNA
422 mutator mice. PLoS ONE *5*, e11468. https://doi.org/10.1371/journal.pone.0011468.

423 Hogan, P.G., Lewis, R.S., and Rao, A. (2010). Molecular Basis of Calcium Signaling in
424 Lymphocytes: STIM and ORAI. Annual Review of Immunology *28*, 491–533.
425 https://doi.org/10.1146/annurev.immunol.021908.132550.

426 Hong, C., and Tontonoz, P. (2014). Liver X receptors in lipid metabolism: opportunities for drug
427 discovery. Nature Publishing Group *13*, 433. https://doi.org/10.1038/nrd4280.

428 Huang, Y.-Y., Gusdon, A.M., and Qu, S. (2013). Cross-talk between the thyroid and liver: A
429 new target for nonalcoholic fatty liver disease treatment. World J Gastroenterol *19*, 8238–8246.
430 https://doi.org/10.3748/wjg.v19.i45.8238.

431 Jakobsson, T., Treuter, E., Ke Gustafsson, J.-A.˚, and Steffensen, K.R. (2012). Liver X receptor
432 biology and pharmacology: new pathways, challenges and opportunities. Trends in
433 Pharmacological Sciences *33*. https://doi.org/10.1016/j.tips.2012.03.013.

434 Jones, B.F., Boyles, R.R., Hwang, S.-Y., Bird, G.S., and Putney, J.W. (2008). Calcium influx
435 mechanisms underlying calcium oscillations in rat hepatocytes. Hepatology *48*, 1273–1281.
436 https://doi.org/10.1002/hep.22461.

437 Kalisky, T., Oriel, S., Bar-Lev, T.H., Ben-Haim, N., Trink, A., Wineberg, Y., Kanter, I., Gilad,
438 S., and Pyne, S. (2018). A brief review of single-cell transcriptomic technologies. Briefings in
439 Functional Genomics *17*, 64–76. https://doi.org/10.1093/bfgp/elx019.

440 Kanoski, S.E., and Grill, H.J. (2017). Hippocampus Contributions to Food Intake Control:
441 Mnemonic, Neuroanatomical, and Endocrine Mechanisms. Biological Psychiatry *81*, 748–756.
442 https://doi.org/10.1016/j.biopsych.2015.09.011.

443 Karakus, E., Wannowius, M., Franz Müller, S., Leiting, S., Leidolf, R., Noppes, S., Oswald, S.,
444 Diener, M., and Geyer, J. The orphan solute carrier SLC10A7 is a novel negative regulator of
445 intracellular calcium signaling. https://doi.org/10.1038/s41598-020-64006-3.

446 Keuper, M., Jastroch, M., Yi, C., Fischer-Posovszky, P., Wabitsch, M., Tschöp, M.H., and
447 Hofmann, S.M. (2014). Spare mitochondrial respiratory capacity permits human adipocytes to
448 maintain ATP homeostasis under hypoglycemic conditions. The FASEB Journal *28*, 761–770.
449 https://doi.org/10.1096/fj.13-238725.

450 Kim, K.S., Seeley, R.J., and Sandoval, D.A. (2018). Signalling from the periphery to the brain
451 that regulates energy homeostasis. Nature Reviews Neuroscience *19*, 185–196.
452 https://doi.org/10.1038/NRN.2018.8.

453 Kimberlin, C.R., Meshcheriakova, A., Palty, R., Raveh, A., Karbat, I., Reuveny, E., and Minor,
454 D.L. (2019). SARAF Luminal Domain Structure Reveals a Novel Domain-Swapped β-Sandwich
455 Fold Important for SOCE Modulation. Journal of Molecular Biology *431*.
456 https://doi.org/10.1016/j.jmb.2019.05.008.

457 Van Der Klaauw, A.A., and Farooqi, I.S. (2015). The hunger genes: Pathways to obesity. Cell
458 *161*, 119–132. https://doi.org/10.1016/j.cell.2015.03.008.

459 Kruse, M.S., Suarez, L.G., and Coirini, H. (2017). Regulation of the expression of LXR in rat
460 hypothalamic and hippocampal explants. Neuroscience Letters *639*, 53–58.
461 https://doi.org/10.1016/j.neulet.2016.12.065.

462 Lebow, M.A., Schroeder, M., Tsoory, M., Holzman-Karniel, D., Mehta, D., Ben-Dor, S., Gil, S.,
463 Bradley, B., Smith, A.K., Jovanovic, T., et al. Glucocorticoid-induced leucine zipper "quantifies"
464 stressors and increases male susceptibility to PTSD. https://doi.org/10.1038/s41398-019-0509-3.

465 Liao, Y., Erxleben, C., Yildirim, E., Abramowitz, J., Armstrong, D.L., and Birnbaumer, L.
466 (2007). Orai proteins interact with TRPC channels and confer responsiveness to store depletion.
467 Proc Natl Acad Sci U S A *104*, 4682–4687. https://doi.org/10.1073/pnas.0611692104.

468 Liou, J., Kim, M.L., Won, D.H., Jones, J.T., Myers, J.W., Ferrell, J.E., and Meyer, T. (2005).
469 STIM is a Ca2+ sensor essential for Ca2+-store- depletion-triggered Ca2+ influx. Current
470 Biology *15*, 1235–1241. https://doi.org/10.1016/j.cub.2005.05.055.

471 Lompré, A.M., Lambert, F., Lakatta, E.G., and Schwartz, K. (1991). Expression of sarcoplasmic
472 reticulum Ca(2+)-ATPase and calsequestrin genes in rat heart during ontogenic development and
473 aging. Circulation Research *69*, 1380–1388. https://doi.org/10.1161/01.RES.69.5.1380.

474 Maron, R., Armony, G., Tsoory, M., Wilchek, M., Frenkel, D., and Arnon, R. Peptide
475 Interference with APP and Tau Association: Relevance to Alzheimer's Disease Amelioration.
476 International Journal of Molecular Sciences Article https://doi.org/10.3390/ijms21093270.

477 Maus, M., Cuk, M., Patel, B., Lian, J., Ouimet, M., Kaufmann, U., Yang, J., Horvath, R.,
478 Hornig-Do, H.-T., Chrzanowska-Lightowlers, Z.M., et al. (2017). Store-Operated Ca2+ Entry
479 Controls Induction of Lipolysis and the Transcriptional Reprogramming to Lipid Metabolism.
480 Cell Metab *25*, 698–712. https://doi.org/10.1016/j.cmet.2016.12.021.

481 McCormick, C.M., and Njeri Ibrahim, F. (2006). Locomotor activity to nicotine and Fos
482 immunoreactivity in the paraventricular nucleus of the hypothalamus in adolescent socially-
483 stressed rats. https://doi.org/10.1016/j.pbb.2006.12.012.

484 Miller, A.M., Asquith, D.L., Hueber, A.J., Anderson, L.A., Holmes, W.M., McKenzie, A.N., Xu,
485 D., Sattar, N., McInnes, I.B., and Liew, F.Y. (2010). Interleukin-33 induces protective effects in
486 adipose tissue inflammation during obesity in mice. Circulation Research *107*, 650–658.
487 https://doi.org/10.1161/CIRCRESAHA.110.218867.

488 Mönnikes, H., Heymann-Mönnikes, I., and Taché, Y. (1992). CRF in the paraventricular nucleus
489 of the hypothalamus induces dose-related behavioral profile in rats. Brain Research *574*, 70–76.
490 https://doi.org/10.1016/0006-8993(92)90801-F.

491 O'Hare, J.D., and Zsombok, A. (2016). Brain-liver connections: Role of the preautonomic PVN
492 neurons. American Journal of Physiology - Endocrinology and Metabolism *310*, E183–E189.
493 https://doi.org/10.1152/ajpendo.00302.2015.

494 Ong, H.L., Subedi, K.P., Son, G.Y., Liu, X., and Ambudkar, I.S. (2019). Tuning store-operated
495 calcium entry to modulate Ca 2+ -dependent physiological processes. Biochimica et Biophysica
496 Acta - Molecular Cell Research *1866*, 1037–1045. https://doi.org/10.1016/j.bbamcr.2018.11.018.

497 Palty, R., Raveh, A., Kaminsky, I., Meller, R., and Reuveny, E. (2012). SARAF inactivates the
498 store operated calcium entry machinery to prevent excess calcium refilling. Cell *149*.
499 https://doi.org/10.1016/j.cell.2012.01.055.

500 Panayotis, N., Sheinin, A., Dagan, S.Y., Tsoory, M.M., Rother, F., Vadhvani, M.,
501 Meshcheriakova, A., Koley, S., Marvaldi, L., Song, D.A., et al. (2018). Importin α5 Regulates
502 Anxiety through MeCP2 and Sphingosine Kinase 1. Cell Reports *25*, 3169-3179.e7.
503 https://doi.org/10.1016/j.celrep.2018.11.066.

504 Parameswaran, R., Morad, V., and Laronne, A. (2008). Targeting the Bone Marrow with Activin
505 A-Overexpressing Embryonic Multipotent Stromal Cells Specifically Modifies B
506 Lymphopoiesis. STEM CELLS AND DEVELOPMENT *17*, 93–105.
507 https://doi.org/10.1089/scd.2007.0099.

508 Park, S.W., Zhou, Y., Lee, J., Lee, J., and Ozcan, U. (2010). Sarco(endo)plasmic reticulum
509 Ca2+-ATPase 2b is a major regulator of endoplasmic reticulum stress and glucose homeostasis
510 in obesity. Proc Natl Acad Sci U S A *107*, 19320–19325.
511 https://doi.org/10.1073/pnas.1012044107.

512 Picard, M., McManus, M.J., Gray, J.D., Nasca, C., Moffat, C., Kopinski, P.K., Seifert, E.L.,
513 McEwen, B.S., and Wallace, D.C. (2015). Mitochondrial functions modulate neuroendocrine,
514 metabolic, inflammatory, and transcriptional responses to acute psychological stress. Proc Natl
515 Acad Sci U S A *112*, E6614-23. https://doi.org/10.1073/pnas.1515733112.

516 Porter, C., Hurren, N.M., Cotter, M. V, Bhattarai, N., Reidy, P.T., Dillon, E.L., Durham, W.J.,
517 Tuvdendorj, D., Sheffield-Moore, M., Volpi, E., et al. (2015). CALL FOR PAPERS Endocrine
518 and Metabolic Dysfunction during Aging and Senescence Mitochondrial respiratory capacity and
519 coupling control decline with age in human skeletal muscle. Am J Physiol Endocrinol Metab
520 *309*, 224–232. https://doi.org/10.1152/ajpendo.00125.2015.-Mitochondrial.

521 Pozzan, T., Rizzuto, R., Volpe, P., and Meldolesi, J. (1994). Molecular and Cellular Physiology
522 of Intracellular Calcium Stores.

523 Prakriya, M., and Lewis, R.S. (2015). STORE-OPERATED CALCIUM CHANNELS. Physiol
524 Rev *95*, 1383–1436. https://doi.org/10.1152/physrev.00020.2014.-Store.

525 Prakriya, M., Feske, S., Gwack, Y., Srikanth, S., Rao, A., and Hogan, P.G. (2006). Orai1 is an
526 essential pore subunit of the CRAC channel. Nature *443*, 230–233.
527 https://doi.org/10.1038/nature05122.

528 Putney, J.W. (1986). A model for receptor-regulated calcium entry. Cell Calcium *7*, 1–12. .

529 Qin, C., Li, J., and Tang, K. (2018a). The paraventricular nucleus of the hypothalamus:
530 Development, function, and human diseases. Endocrinology *159*, 3458–3472.
531 https://doi.org/10.1210/en.2018-00453.

532 Qin, C., Li, J., and Tang, K. (2018b). The paraventricular nucleus of the hypothalamus:
533 Development, function, and human diseases. Endocrinology *159*, 3458–3472.
534 https://doi.org/10.1210/en.2018-00453.

535 Roh, E., Song, D.K., and Kim, M.S. (2016). Emerging role of the brain in the homeostatic
536 regulation of energy and glucose metabolism. Experimental and Molecular Medicine *48*, 216.
537 https://doi.org/10.1038/emm.2016.4.

538 Romanuik, T.L., Ueda, T., Le, N., Haile, S., Yong, T.M.K., Thomson, T., Vessella, R.L., and
539 Sadar, M.D. (2009). Novel biomarkers for prostate cancer including noncoding transcripts. Am J
540 Pathol *175*, 2264–2276. https://doi.org/10.2353/ajpath.2009.080868.

541 Roos, J., Digregorio, P.J., Yeromin, A. V, Ohlsen, K., Lioudyno, M., Zhang, S., Safrina, O.,
542 Kozak, J.A., Wagner, S.L., Cahalan, M.D., et al. (2005). STIM1, an essential and conserved
543 component of store-operated Ca 2 channel function. The Journal of Cell Biology *169*, 435–445.
544 https://doi.org/10.1083/jcb.200502019.

545 Ruggiero, A., Aloni, E., Korkotian, E., Zaltsman, Y., Oni-Biton, E., Kuperman, Y., Tsoory, M.,
546 Shachnai, L., Levin-Zaidman, S., Brenner, O., et al. (2017). Loss of forebrain MTCH2 decreases
547 mitochondria motility and calcium handling and impairs hippocampal-dependent cognitive
548 functions. Scientific Reports *7*, 1–13. https://doi.org/10.1038/srep44401.

549 La Russa, D., Frisina, M., Secondo, A., Bagetta, G., and Amantea, D. (2020). Modulation of
550 cerebral store-operated calcium entry-regulatory factor (SARAF) and peripheral Orai1 following
551 focal cerebral ischemia and preconditioning in mice. Neuroscience
552 https://doi.org/10.1016/j.neuroscience.2020.06.014.

553 Sabourin, J., Le Gal, L., Saurwein, L., Haefliger, J.A., Raddatz, E., and Allagnat, F. (2015).
554 Store-operated Ca2+ entry mediated by Orai1 and TRPC1 participates to insulin secretion in rat
555 β-cells. Journal of Biological Chemistry *290*, 30530–30539.
556 https://doi.org/10.1074/jbc.M115.682583.

557 Sanlialp, A., Schumacher, D., Kiper, L., Varma, E., Riechert, E., Ho, T.C., Hofmann, C.,
558 Kmietczyk, V., Zimmermann, F., Dlugosz, S., et al. (2020). Saraf-dependent activation of
559 mTORC1 regulates cardiac growth. Journal of Molecular and Cellular Cardiology
560 https://doi.org/10.1016/j.yjmcc.2020.03.004.

561 Schindelin, J., Arganda-Carreras, I., Frise, E., Kaynig, V., Longair, M., Pietzsch, T., Preibisch,
562 S., Rueden, C., Saalfeld, S., Schmid, B., et al. (2012). Fiji: an open-source platform for
563 biological-image analysis. Nature Methods 2012 9:7 *9*, 676–682.
564 https://doi.org/10.1038/nmeth.2019.

565 Shimizu, I., and Walsh, K. (2015). The Whitening of Brown Fat and Its Implications for Weight
566 Management in Obesity. Curr Obes Rep *4*, 224–229. https://doi.org/10.1007/s13679-015-0157-8.

567 Snyder, J.S., Soumier, A., Brewer, M., Pickel, J., and Cameron, H.A. (2011). Adult hippocampal
568 neurogenesis buffers stress responses and depressive behaviour. Nature *476*, 458–461.
569 https://doi.org/10.1038/nature10287.

570 Son, A., Ahuja, M., Schwartz, D.M., Varga, A., Swaim, W., Kang, N., Maleth, J., Shin, D.M.,
571 and Muallem, S. (2019). Ca2+ Influx Channel Inhibitor SARAF Protects Mice From Acute
572 Pancreatitis. Gastroenterology https://doi.org/10.1053/J.GASTRO.2019.08.042.

573 Srivats, S., Balasuriya, D., Pasche, M., Vistal, G., Michael Edwardson, J., Taylor, C.W., and
574 Murrell-Lagnado, R.D. (2016). Sigma1 receptors inhibit store-operated Ca2+ entry by
575 attenuating coupling of STIM1 to Orai1. Journal of Cell Biology
576 https://doi.org/10.1083/jcb.201506022.

577 Stiber, J., Hawkins, A., Zhang, Z.-S., Wang, S., Burch, J., Graham, V., Ward, C.C., Seth, M.,
578 Finch, E., Malouf, N., et al. (2008). STIM1 signaling controls store operated calcium entry
579 required for development and contractile function in skeletal muscle. Nat Cell Biol *10*, 688–697.
580 https://doi.org/10.1038/ncb1731.

581 Tagliaferri, M., Berselli, M.E., Calò, G., Minocci, A., Savia, G., Petroni, M.L., Viberti, G.C., and
582 Liuzzi, A. (2001). Subclinical Hypothyroidism in Obese Patients: Relation to Resting Energy
583 Expenditure, Serum Leptin, Body Composition, and Lipid Profile. Obesity Research *9*, 196–201.
584 https://doi.org/10.1038/oby.2001.21.

585 Tamarina, N.A., Kuznetsov, A., Rhodes, C.J., Bindokas, V.P., and Philipson, L.H. (2005).
586 Inositol (1,4,5)-trisphosphate dynamics and intracellular calcium oscillations in pancreatic β-
587 cells. Diabetes *54*, 3073–3081. https://doi.org/10.2337/diabetes.54.11.3073.

588 Thornton, A.M., Zhao, X., Weisleder, N., Brotto, L.S., Bougoin, S., Nosek, T.M., Reid, M.,
589 Hardin, B., Pan, Z., Ma, J., et al. (2011). Store-Operated Ca2+ Entry (SOCE) contributes to
590 normal skeletal muscle contractility in young but not in aged skeletal muscle. Aging *3*, 621–634.
591 https://doi.org/10.18632/aging.100335.

592 Toescu, E.C., and Verkhratsky, A. (2007). The importance of being subtle: Small changes in
593 calcium homeostasis control cognitive decline in normal aging. Aging Cell *6*, 267–273.
594 https://doi.org/10.1111/j.1474-9726.2007.00296.x.

595 Traba, J., Miozzo, P., Akkaya, B., Pierce, S.K., and Akkaya, M. (2016). An Optimized Protocol
596 to Analyze Glycolysis and Mitochondrial Respiration in Lymphocytes. J Vis Exp
597 https://doi.org/10.3791/54918.

598 Uyama, N., Geerts, A., and Reynaert, H. (2004). Neural connections between the hypothalamus
599 and the liver. The Anatomical Record *280A*, 808–820. https://doi.org/10.1002/ar.a.20086.

600 Waters, D.L., Brooks, W.M., Qualls, C.R., and Baumgartner, R.N. (2003). Skeletal muscle
601 mitochondrial function and lean body mass in healthy exercising elderly. Mechanisms of Ageing
602 and Development *124*, 301–309. https://doi.org/10.1016/S0047-6374(02)00197-5.

603 Wei-Lapierre, L., Carrell, E.M., Boncompagni, S., Protasi, F., and Dirksen, R.T. (2013). Orai1-
604 dependent Calcium Entry Promotes Skeletal Muscle Growth and Limits Fatigue. Nature
605 Communications https://doi.org/10.1038/ncomms3805.

606 Wilson, C.H., Ali, E.S., Scrimgeour, N., Martin, A.M., Hua, J., Tallis, G.A., Rychkov, G.Y., and
607 Barritt, G.J. (2015). Steatosis inhibits liver cell store-operated Ca^{2+} entry and reduces ER Ca^{2+}
608 through a protein kinase C-dependent mechanism. Biochem J *466*, 379–390.
609 https://doi.org/10.1042/BJ20140881.

610 Wolf, Y., Boura-Halfon, S., Cortese, N., Haimon, Z., Sar Shalom, H., Kuperman, Y., Kalchenko,
611 V., Brandis, A., David, E., Segal-Hayoun, Y., et al. (2017). Brown-adipose-tissue macrophages
612 control tissue innervation and homeostatic energy expenditure. Nature Immunology
613 https://doi.org/10.1038/ni.3746.

614 Yeromin, A. V., Zhang, S.L., Jiang, W., Yu, Y., Safrina, O., and Cahalan, M.D. (2006).
615 Molecular identification of the CRAC channel by altered ion selectivity in a mutant of Orai.
616 Nature *443*, 226–229. https://doi.org/10.1038/nature05108.

617 Zhao, G., Li, T., Brochet, D.X.P., Rosenberg, P.B., and Lederer, W.J. (2015). STIM1 enhances
618 SR Ca2+ content through binding phospholamban in rat ventricular myocytes. Proc Natl Acad
619 Sci U S A *112*, E4792–E4801. https://doi.org/10.1073/pnas.1423295112.

620 Zhao, X., Weisleder, N., Thornton, A., Oppong, Y., Campbell, R., Ma, J., and Brotto, M. (2008).
621 Compromised store-operated Ca2+ entry in aged skeletal muscle. Aging Cell *7*, 561–568.
622 https://doi.org/10.1111/j.1474-9726.2008.00408.x.

623

624

625

626 **Materials and methods:**

627 **Mice**

628 The SARAF conditional KO strain used for this research project was generated from KOMP ES
629 cell line *Saraf*$^{tm1a(KOMP)Wtsi}$, RRID:MMRRC_061775-UCD, was obtained from the Mutant Mouse
630 Resource and Research Center (MMRRC) at University of California at Davis, an NIH-funded
631 strain repository, and was donated to the MMRRC by The KOMP Repository (University of
632 California, Davis); Originating from Pieter de Jong, Kent Lloyd, William Skarnes, Allan Bradley,
633 Wellcome Sanger Institute. The ES cells were created by introducing a splice acceptor/reporter
634 cassette containing a poly-A site into an endogenous intron upstream of a critical exon. The
635 cassette includes the lacZ gene and the neomycin resistance gene surrounded by FLP sites, and the
636 critical (third) SARAF exon floxed by loxP sites (Fig. 1A). The following Jackson laboratory mice
637 lines were used for crossing and generation of conditional mice lines:
638 Gt(ROSA)26Sortm1(FLP1)Dym, Tg(Pgk1-cre)1Lni, B6.FVB(129X1) Tg(Sim1-cre)1Lowl/J. All
639 general and spatially specific SARAF knocked-out mice were compared to their wild-type
640 littermates.
641 All the animal procedures were approved by the Weizmann Institute Institutional Animal Care and
642 Use Committee (IACUC).
643

644 **Genotyping**

645 Genomic DNA was isolated from a tail biopsy using 25mM NaOH and 0.2mM disodium EDTA
646 extraction buffer (PH12) incubated for 1 h at 95°C, the extract was neutralized using 40mM Tris-
647 HCl neutralization buffer (PH5), and PCR identified mouse genotypes. Two PCR primers were
648 synthesized to detect the intact *Cre* gene; three PCR primers were synthesized to detect the KOMP,
649 WT, and loxp inserted SARAF gene, and four PCR primers were used to detect WT, KO, and HET
650 mice in the SARAF$^{fl/fl}$PGKCre line. The PCR conditions were 95°C denaturing, 60°C (for
651 SARAF) 55°C (for Cre) 65°C (for SARAF$^{fl/fl}$PGKCre) annealing, and 72°C extension for 35
652 cycles using Taq polymerase and a DNA Thermal Cycler from Bio-Rad. The PCR products were
653 resolved by electrophoresis in 1% agarose gel.

654 **Mouse embryonic fibroblasts (MEFs)**

655 E14.5 embryos were dissected, and their trunks were extracted into cold PBS. The trunks were
656 finely minced using a razor until they were pipettable. Cells were suspended in 3ml trypsin-EDTA
657 0.05%, at 37C for 10 min. Cells were flushed through 21g (3ml) syringe three times, and double
658 serum levels to block the trypsin activity. Next, cells were centrifuged at 1800 rpm for 5 min, and
659 the pellet re-suspended in 8 ml of MEF media, containing 10% fetal calf serum, 2% Penstrep, 1%
660 L-glutamine, and 1% sodium pyruvate. Cells from each embryo were plated on a 100mm dish
661 coated with 0.1% gelatin. Cells were split 1:4 and frozen when they reached confluence
662 (Parameswaran et al., 2008).

663 **Primary hepatocyte**

664 Mouse hepatocytes were isolated from 8–12 weeks old male mice. Mice were anesthetized using
665 ketamine and xylazine, liver was exposed and perfused by two steps, wash and a digestion step
666 was done by Liberase research-grade (Roche Diagnostics). Cells were centrifuged in Percoll (GE
667 Healthcare) gradient and seeded on Collagen type 1 (Sigma) coated plates with HBM basal
668 medium+ HCM single Quotes (Lonza) media containing 1% FBS for 2.5–3 h, later washed with
669 non-serum containing media and used for experiments for up to 24 hours (Halpern et al., 2018).

670 **Primary hippocampal cultures**

671 Cultures were prepared from E18-P0 mouse pups, pups were decapitated, their brains removed,
672 and the hippocampi dissected free and placed in chilled (4°C), oxygenated Leibovitz L15 medium
673 (Gibco, Gaithersburg, MD, USA). The hippocampi were dissociated mechanically, and cells were
674 plated in 24-well plate, onto round coverslips coated with L-polylysine. Glia plated 14 days
675 beforehand and grown in 10%FBS and Glutamate. Cultures grew in a medium containing 5% HS,
676 5% FBS and B27 in an incubator at 37 °C with 5% CO2. Cells were imaged at 13–17 days after
677 plating.

678 **Behavioral assays**

679 All behavioral assays were performed during the dark period (08:00–20:00) in a reverse cycle
680 room. Before each experiment, mice were habituated to the test room for two hours.

681 Morris water maze: For the acquisition phase, mice were subjected to 4 trials per day with an
682 interval of 15 mins, for 7 consecutive days. In each trial, the mice were required to find a hidden
683 platform located 1 cm below the water surface in a 120 cm-diameter circular pool. In the testing

684 room, only distal visual-spatial cues for locating the hidden platform were available. The escape
685 latency in each trial was recorded up to 90s. Each mouse was allowed to remain on the platform
686 for 15s and was then removed from the maze. If the mouse did not find the platform within the
687 90s, it was manually placed on it for 15s. Memory was assessed 24 hours after the last trial. The
688 escape platform was removed, and mice were allowed to search for it for 1 minute, and the time
689 spent in the different quadrants of the pool was recorded using a VideoMot2 automated tracking
690 system (Tse-System)(Panayotis et al., 2018; Ruggiero et al., 2017).

691 Y-maze: The maze contains three arms at 120 degrees to each other. The mouse underwent training
692 and test on the same day. During training, one arm was closed. During the test, the mouse starts at
693 the end of one arm and then chooses between the other two arms. The amount of time and duration
694 spent in the closed arm is measured to demonstrate learning and memory (Maron et al.).

695 Dark-light transfer test: The test consists of a polyvinyl chloride box divided into a dark black
696 compartment (14 × 27 × 26 cm) and a white 1050-lx illuminated light compartment (30 × 27 × 26
697 cm) connected by a small passage. Mice were placed in the dark compartment to initiate a 5-min
698 test session. The time spent in the light compartment and the number of entries to the light
699 compartment were measured.

700 Acoustic startle response: Mice were placed in a small Plexiglas mesh cage on top of a vibration-
701 sensitive platform in a sound-attenuated, ventilated chamber. A high-precision sensor integrated
702 into the measuring platform detected the movement. Two high-frequency loudspeakers inside the
703 chamber produced all the audio stimuli. The acoustic startle response session began with 5 min
704 acclimatization to white background noise [65 dB] maintained throughout the session. Thirty-two
705 startle stimuli [120 dB, 40ms duration with a randomly varying ITI of 12–30s] were presented.
706 The reaction time and latency to peak startle amplitude were measured (Panayotis et al., 2018).

707 **Immunohistochemistry**

708 The mice were anesthetized and perfused with 1% PFA in PBS. Brains were carefully removed
709 and fixed overnight in 30% sucrose 1% PFA in PBS. The following day 30 µm coronal slices were
710 prepared using a sliding microtome and stored in PBS 0.01% Na-Azid.

711 For X-gal staining, the 30 µm slices were incubated in PBS containing 1% glutaraldehyde for 4
712 min and washed three times in PBS. Slices were incubated overnight in X-gal staining solution

713 containing 3 mM $K_3Fe(CN)_6$, 3 mM $K_4Fe(CN)_6$, 1.3 mM $MgCl_2$, 0.02% NPO_4, 0.01% NaDOC
714 and 1 mg/ml X-gal in PBS, filtered through a 0.45 μM filter. The next day slices were washed
715 three times in PBS and mounted on slides.

716 For immunohistochemistry, the following primary antibodies were used: rabbit anti-beta-
717 galactosidase (1:1000; Cappel), goat anti-doublecortin (1:100; Santa Cruz). Slices/cells were first
718 incubated for 1.5 h at room temperature in a blocking solution containing 20% normal horse serum
719 (NHS) and 0.3% triton x100 in PBS, followed by 48–72 h incubation at 4°C in primary antibody
720 solution containing 2% NHS and 0.3% triton x100 in PBS. The slices were then washed with PBS
721 and incubated with biotin-conjugated goat anti-rabbit (1:200; Jackson) in 2% NHS-PBS for 1.5 h
722 at room temperature. Finally, slices were incubated for 1 h at room temperature with secondary
723 antibody FITS -conjugated donkey anti-goat (1:200; Jackson) and Cy3-streptavidin (1:200;
724 Jackson). Slices were then washed with PBS and incubated for 10min with Hoechst (1:2000),
725 washed and mounted for fluorescence imaging.

726 Cells were fixed with 4% PFA in PBS for 15 min, washed, and permeabilized using 0.2% triton
727 x100 in PBS for 30 min. Cells were blocked for 1.5 h, with 5% horse serum in PBS. The primary
728 rabbit anti Ki67 (1:200, Abcam) antibody was incubated overnight. Secondary goat anti-rabbit cy3
729 (1:200, Jackson) antibody was incubated for 30 min. Cells were then washed with PBS and
730 incubated for 10min with Hoechst (1:2000), washed and mounted for fluorescence imaging.

731 EdU-proliferating cells staining mice were given 0.2 mg/ml EdU (CarboSynth) in drinking water
732 for two weeks and then sacrificed. Brains were embedded in paraffin, and hippocampal slices were
733 then used for immunostaining, using the Click-iT EdU imaging kit (Invitrogen). Staining was done
734 according to manufacturer instructions.

735 **Rabbit polyclonal anti-SARAF antibody production**

736 Rabbit polyclonal anti SARAF antibody production was performed with the help of the
737 Weizmann institute core facilities, antibody engineering unit. Two NZW SPF rabbits (New
738 Zealand White rabbits) were subcutaneously injected with SARAF's luminal domain (aa 30–
739 164) fused to 6xHistidine tag (Kimberlin et al., 2019). The first injection was done with Freund's
740 complete adjuvant (Difco 263810), and the second was given a week later with Freund's
741 incomplete adjuvant (263910). Three boosters with an interval of 14 days were given IP in PBS,

742 and serum was collected after each boost. The serums were purified for mouse IgG subclasses by
743 affinity chromatography on protein-A Sepharose beads CL-4B (SPA-Sepharose, Pharmacia,
744 Sweden). The best serum of the two was selected (according to western blotting), and additional
745 purification steps were conducted as follows: rabbit serum was filtered using a 0.2mM filter
746 (Nalgene) and loaded onto the affinity HisTrap-NHS column. The column was washed by 10CV
747 PBS, 15CV washing buffer, and an additional 10CV PBS. The first elution step was performed
748 with a Glycine buffer (0.1M Glycine titrated to pH 2.3 with HCl). The second elution step was
749 then done using the 5CV of TEA (Tetra-Ethyl-Ammonium) pH 11.5 (titrated with NaOH). The
750 second fraction, eluted under basic conditions, had superior selectivity and specificity compared
751 to the total serum and wad used for western blot analysis. All columns used are commercially
752 available as pre-packed media from GE healthcare.

753 **Western blot**

754 Protein was extracted from adult mice brains in sucrose extraction buffer containing 0.32 M
755 sucrose, 2mM EDTA, 10mM HEPES pH=7.4, PMSF (1:100), and protease inhibitor cocktail
756 (1:50). Extracts were then homogenized on ice with glass homogenizer, centrifuged at 750g for 10
757 min to remove crude debris, then ultracentrifuged at 200,000 g for 40 min, pellet re-suspended in
758 CL47a complexiolyte solubilization buffer (Logopharm) and kept for 30 min on ice and then used
759 for protein quantification with Pierce BCA kit (Thermo Fisher). Protein lysates were
760 electrophoresed on a 10% SDS–polyacrylamide gel electrophoresis (SDS-PAGE), transferred to
761 nitrocellulose membranes, blocked and treated overnight with a rabbit polyclonal anti-SARAF
762 (1:5000), in PBS containing 0.05% tween (PBST) with 1% BSA. After washing, the membranes
763 were incubated with horseradish peroxidase-conjugated goat anti-rabbit IgG antibody (Jackson) in
764 PBST with 2.5% skim milk. Electrochemiluminescence (ECL) detected the immunoreactive
765 protein (WesternBright ECL HRP substrate, Advansta).

766 **Corticosteroid blood measurements**

767 Corticosterone was measured 5 h after the dark cycle begun using the DetectX Corticosterone
768 CLIA kit (Arbor assays). 5µl tail blood samples from mice were collected before (basal),
769 immediately after 15 min of restraint stress, 30 and 75 min from stress initiation. The restraint
770 stress was induced using a cut 50-ml plastic conical tube. Plasma samples were immediately

771 centrifuged and stored at −80 °C until assays for hormone measurement were conducted. Blood
772 was analyzed according to manufacture instructions (Lebow et al.).

773 **micro-CT**

774 Mice were anesthetized with isoflurane (3% for induction, 1%–2% for maintenance) mixed with
775 oxygen (1 l/min) and delivered through a nasal mask. Once anesthetized, the mice were placed in
776 a head-holder to assure reproducible positioning inside the scanner. The set of mice were scanned
777 using a micro-CT device TomoScope® 30S Duo scanner (CT Imaging, Germany) equipped with
778 two source-detector systems. The operation voltages of both tubes were 40 kV. The integration
779 time of protocols was 90 ms (360 rotation) for 3 cm length, and axial images were obtained at an
780 isotropic resolution of 80 µ. Due to the maximum length limit, to cover the entire mouse body,
781 imaging was performed in two parts with the overlapping area, and then all slices merged to one
782 dataset representing the entire ROI. The radiation dose for each mouse was 2.2 Gy(Akselrod-Ballin
783 et al., 2016). Fat quantification analysis was performed using a CT analysis (skyscan Bruker
784 MicroCT) software (Version1.19).

785 **Calcium Imaging**

786 Cells were plated onto 24 mm L-polylysine coated cover glass 4-24 h before the experiment.
787 Before the experiment, the cover glass was mounted on an imaging chamber and washed with a
788 0/2mM Ca^{2+} solution. Fura-2AM loading of cells was performed for 30-45 minutes. Cytosolic
789 Ca^{2+} levels were recorded from Fura-2AM-loaded cells, excited at wavelengths of 340/20 and
790 380/20 nm and imaged with 510/80 nm filters. For all single-cell imaging experiments, traces of
791 averaged responses, recorded from 10 to 50 cells.

792 Cells were stimulated with ATP (100mM), carbachol (100mM) and bradykinin (1.5mM) in
793 100mg/ml BSA or with S-DHPG (10mM)/Vasopressin(1nM) and SOCE was induced by 2-5mM
794 of Ca^{2+}. Additionally, cells were washed with 0mM Ca^{2+} and stores were emptied by thapsigargin
795 (2mM)/BHQ (20mM) and SOCE was again induced by 2-5mM Ca^{2+}. All materials were purchased
796 from Sigma and diluted in 0/2mM Ca^{2+} solution. Solutions used for imaging were either standard
797 Ringer's solution with or without $CaCl_2$ or solutions with the following constituents: 0mM Ca^{2+}
798 solution contained HBSS-/-, 20mM Hepes, 1mM $MgCl_2$, 0.5mM EGTA and glucose calibrated to

799 PH=7. 2-5 mM Ca^{2+} solution contained the same except for the absence of EGTA and addition of
800 2-5 mM $CaCl_2$(Kimberlin et al., 2019; Palty et al., 2012).

801 **Murine metabolic studies**

802 Indirect calorimetry, food, water intake, and locomotor activity were measured using the
803 LabMaster system (TSE-Systems, Bad Homburg, Germany). Data were collected after 48h of
804 adaptation from singly housed mice. Body composition was assessed using the Bruker minispec
805 mq7.5 live mice analyzer (Wolf et al., 2017).

806 **Running wheel**

807 Mice were singly housed in standard cages equipped with a running wheel for four weeks
808 (Colombus Instruments). Distances were recorded every 15 min from a counter attached to the
809 wheel. The wheel circumference (111.76 cm) was converted to kilometers.

810 **Cellular respiration**

811 Measurement of intact cellular respiration was performed using the Seahorse XF24 analyzer
812 (Seahorse Bioscience Inc.) and the XF Cell Mito Stress Test Kit according to the manufacturer's
813 instructions. Respiration was measured under basal conditions, and in response to Oligomycin
814 (ATP synthase inhibitor; 0.5 μM) and the electron transport chain accelerator ionophore, FCCP
815 (trifluorocarbonylcyanide phenylhydrazone;1 μM), to measure the maximal oxygen consumption
816 rate (OCR). Finally, respiration was stopped by adding the electron transport chain inhibitor
817 AntimycinA (1 μM) (Ruggiero et al., 2017).

818 **Glucose tolerance test.**

819 Mice were fasted for five hours and subsequently given 2g/kg glucose solution by i.p. injection.
820 Blood glucose was determined at 0, 15, 30, 60, 90, and 120 min after the glucose challenge
821 (FreeStyle Freedom Lite, Abbott)(Wolf et al., 2017).

822 **RNA sequencing**

823 Total RNA was extracted from the indicated cell cultures using the RNeasy kit (QIAGEN).
824 Then, RNA integrity was evaluated on a Bioanalyzer (Agilent 2100 Bioanalyzer), requiring a
825 minimal RNA integrity number (RIN) of 8.5. Libraries were prepared according to Illumina's
826 instructions accompanying the TruSeq RNA Sample Preparation Kit v2 (cat # RS-122–2001).

827 According to the manufacturer's instructions, sequencing was carried out on Illumina HiSeq
828 2500v4 SR60, 20 million reads per sample.

829 Sequenced reads were mapped to the Mus musculus genome version GRCm38, using TopHat
830 v2.0.10. Genes were identified using a.gtf obtained from Ensembl release 82. Per gene, reads were
831 counted using HTSeq. Normalization of read counts and P-values for differentially expressed
832 genes were computed using DESeq2(Kalisky et al., 2018).

833 **Statistical and image analysis**

834 Images were analyzed and quantified using the Fiji/ImageJ software.

835 P-values were calculated using a student's t-test for statistical comparisons of mean values using
836 the GraphPad Prism software. Differences were regarded significant for $p<0.05$ (*) and highly
837 significant for $p<0.01$ (**) and $p<0.001$(***).

838

839 # STAR methods

840 Key resources table

Reagent or resource	source	identifier
Antibodies		
rabbit anti-beta-galactosidase	MP bio(Cappel)	Cat# 0855976 AB_2334934
goat anti-doublecortin	Santa Cruz	Cat# sc-8066 AB_2088494
biotin-conjugated goat anti-rabbit	Jackson laboratories	Cat# 111-065-003 AB_2337959
FITS -conjugated donkey anti-goat	Jackson laboratories	Cat# 705-095-147 AB_2340401
Cy3-strepavidin	Jackson laboratories	Cat# 016-160-084 AB_2337244
Rabbit anti Ki67	Abcam	Cat# ab15580 AB_443209
Cy3 goat anti-rabbit	Jackson laboratories	Cat# 111-165-003 AB_2338000
Rabbit polyclonal anti-SARAF	This paper	N/A
Peroxidase Goat Anti-Rabbit IgG	Jackson laboratories	Cat# 111-035-144 AB_2307391
Chemicals, Peptides, and Recombinant Proteins		
Hoechst 33342	Life Technologies	Cat# H3570
X-gal	Thermo Scientific	Cat#R0404
Pierce™ 16% Formaldehyde	Thermo Scientific	Cat#28906
DMEM - Dulbecco's Modified Eagle Medium Gibco™	Thermo Scientific	Cat#41965-039
Fetal bovine serum Gibco™	Thermo Scientific	Cat#10270-106
Dulbecco's Phosphate Buffered Saline	Biological industries (Sartorius)	Cat#02-023-1A
L-Glutamine solution	Biological industries (Sartorius)	Cat#03-020-1B
Sodium pyruvate solution	Biological industries (Sartorius)	Cat#03-042-1B

Pen-Strep solution	Biological industries (Sartorius)	Cat#03-031-1B
Trypsin-EDTA solution	Biological industries (Sartorius)	Cat#03-050-1B
Leibovitz L15 medium Gibco™	Thermo Scientific	Cat#11415064
MEM without L-glutamine Gibco™	Thermo Scientific	Cat#21090-022
Gentamicin	Sigma-Aldrich(Merck)	Cat#G-1272
Glutamax Gibco™	Thermo Scientific	Cat#35050-038
Horse serum Gibco™	Thermo Scientific	Cat#26050-047
FUDR	Sigma-Aldrich(Merck)	Cat#F-0503
Uridine	Sigma-Aldrich(Merck)	Cat#U-3750
B27 supplements Gibco™	Thermo Scientific	Cat#7504-010
0.1% Gelatine	Biological industries	Cat#01-944-1B
Taq DNA Polymerase 2x Master Mix RED	Ampliqon	Cat# A190303
Liberase research-grade	Roche Diagnostics	Cat#5401119001
Percoll	Cytiva (GE Healthcare)	Cat#17089102
Bovine serum albumin, fraction V	MP	Cat#160069
Collagen, Type I solution from rat tail	Sigma-Aldrich(Merck)	Cat#C3867
HBM ™ basal medium	Lonza	Cat#CC-3199
HCM™ SingleQuots™ Kit	Lonza	Cat#CC-4182
Leibovitz L15 medium Gibco™	Thermo Scientific	Cat#11415064
Poly-L-lysine solution	Sigma-Aldrich(Merck)	Cat#P4707

2'-Deoxy-5-ethynyluridine (5-EdU)	CarboSynth	Cat#NE08701
Freund's complete adjuvant	Difco	Cat#263810
Freund's incomplete adjuvant	Difco	Cat#263910
protein-A Sepharose beads CL-4B	Cytiva (GE Healthcare)	Cat#GE17-0780-01
cOmplete™, Mini Protease Inhibitor Cocktail	Roche	Cat#11836153001
CL47a complexiolyte solubilization buffer	Logopharm	N/A
Fura-2AM Calbiochem	Sigma-Aldrich(Merck)	Cat#108964-32-5
carbachol	Sigma-Aldrich(Merck)	Cat#51-83-2
Bradykinin acetate salt	Sigma-Aldrich(Merck)	Cat#B3259
(S)-3,5-DHPG	Tocris	Cat#0805
Vasopressin	Sigma-Aldrich(Merck)	Cat#113-79-1
Thapsigargin	Alomone labs	Cat# T-650
BHQ Calbiochem	Sigma-Aldrich(Merck)	Cat#286888
Critical Commercial Assays		
Click-iT EdU imaging kit	Invitrogen	Cat#C10339
Pierce ™ BCA kit	Thermo Fisher	Cat#23225
WesternBright ECL HRP substrate	Advansta	Cat#K-12045-D20
DetectX corticosterone CLIA kit	Arbor assays	Cat#K014-C1
XF Cell Mito Stress Test Kit	Agilent	Cat#103015-100
RNeasy kit	QIAGEN	Cat#74104
TruSeq RNA Sample Preparation Kit v2	ILUMINA	Cat# RS-122–2001
Deposited Data Submitted to GEO -GSE193354 https://www.ncbi.nlm.nih.gov/geo/query/acc.cgi?acc=GSE193354		
RNA-seq data	This paper	

Experimental Models: Cell Lines		
Saraf^{tm1a}(KOMP)Wtsi ES clone	EUCOMM/KOMP	061775-UCD
Mouse embryonic fibroblasts (MEFs)	This paper	N/A
Primary hepatocytes	This paper	N/A
Primary hippocampal cultures	This paper	N/A
Experimental Models: Organisms/Strains		
SARAF$^{fl/fl}$	This paper	N/A
Gt(ROSA)26Sortm1(FLP1)Dym	The Jackson Laboratory	#003946
Tg(Pgk1-cre)1Lni	The Jackson Laboratory	#020811
B6.FVB(129X1) Tg (Sim1-cre)1Lowl/J	The Jackson Laboratory	#006451
NZW SPF rabbits	ENVIGO	N/A
Oligonucleotides		
Primer: Cre Forward: GGCCAGCTAAACATGCTTCA	This paper	N/A
Primer: Cre Reverse: ACACCAGAGACGGAAATCCATC	This paper	N/A
Primer: KO Forward: GGAACTTCGTCGAGATAACTTCGTATAGCATAC	This paper	N/A
Primer: WT Forward: ACAGGATGTACCTATGACAACAGTGGCAAT	This paper	N/A
Primer: Reverse WT: TAGACTCATGAATTTGAATGCCTGGCCC	This paper	N/A
Primer: PGK Forward 5546: CCCGACCCCTACAACACGTA	This paper	N/A
Primer: Reverse 5747: CACCACTCGACACTTCCGAT	This paper	N/A
Primer: Reverse 6290: CAGACTCGAGCGGTAGTCAAGTAGT	This paper	N/A

Software and Algorithms		
VideoMot2 automated tracking system	TSE-Systems	https://www.tse-systems.com/service/videomot2/
PhenoMaster system	TSE-Systems	https://www.tse-systems.com/service/phenomaster/
FIJI/Image J	Schindelin et al., 2012(Schindelin et al., 2012)	https://fiji.sc/
Prism	GraphPad	https://www.graphpad.com/scientific-software/prism/
SlideViewer 2.5	3DHISTECH	https://www.3dhistech.com/research/software-downloads/
Inskape 1.1.1	Inskape	https://inkscape.org/
Wave Controller Software 2.6 for XF24 analyzer	Seahorse Bioscience	https://www.agilent.com/en/product/cell-analysis/real-time-cell-metabolic-analysis/xf-software/seahorse-wave-controller-software-2-6-1-740904
Ingenuity® pathway analysis	QIAGEN	https://digitalinsights.qiagen.com/products-overview/discovery-insights-portfolio/analysis-and-visualization/qiagen-ipa/

846 **Figure legends**

847 **Figure 1: Generation of SARAF conditional mice, SARAF expression in the brain and**
848 **SARAF$^{fl/fl}$ PGK-Cre^{+} metabolic phenotype. A,** Schematic representation of the SARAF knock-
849 in cassette and after flipase exertion of the cassette leaving crucial exon 3 flanked by loxP sites. **B**,
850 X-gal-stained coronal brain sections of KOMP cassette-inserted heterozygous mice, expressing β-
851 gal at the sites of SARAF expression (scale bar 1mm). **C**, Changes in body weight of SARAF-WT
852 (n=13, blue) and SARAF-KO (n=11, red) over time. Inset, representative photos of SARAF-WT
853 (right) and SARAF-KO (left) mice at 1-years-old. **D**, Lean and fat mass percentage of SARAF-
854 WT (n=13, blue) and SARAF-KO (n=11, red) mice at 3-months and 1 years old. **E-F**, PhenoMaster
855 calorimetry metabolic analysis of 3-month-old mice (SARAF-WT, n=8; SARAF-KO, n=10). E.
856 Heat production over time. **F,** Dark-phase locomotion. **G**, Total food intake. **H,** three- months old
857 mice glucose tolerance test ((SARAF-WT, n=7; SARAF-KO, n=9).

858 **Figure 2: Characterization of SARAF-KO lipid deposition phenotype and voluntary training**
859 **treatment. A,** Micro-CT imaging and whole-body fat (right) distribution analysis of representative
860 1-year-old SARAF-WT and SARAF-KO mice. **B**, Abdominal fat representative images of CT
861 images of above-mentioned mice. **C**, Quantification of visceral fat deposition. **D**, Inguinal WAT,
862 visceral WAT, liver and iBAT tissue histology in 1-years-old SARAF-WT and SARAF-KO mice.
863 Size bar-100 μm. **E-F**, Inguinal, and visceral WAT droplet size quantification. **G-H**, iBAT, and
864 liver pixels of fat droplets/area quantification. **I,** Serum analysis of cholesterol levels of 1 year-old
865 mice. **J**, Serum analysis of thyroxine levels 1 year-old mice. **K**, Serum analysis of TSH levels of
866 1 year-old mice.

867 **Figure 3**: **SARAF-SIM1KO mice metabolic related phenotypes. A**, three-months, and 1-year
868 old SARAF-SIM1WT (n=16) and SARAF-SIM1KO (n=9) mice body weight comparison. **B**, Lean
869 and fat mass percentage SARAF-SIM1WT and SARAF-SIM1KO three-months and one-year old
870 mice of the same mice as in A. **C**, Three-months-old glucose tolerance test (SARAF-SIM1WT,
871 n=11; SARAF-SIM1KO, n=6). **D-F**, PhenoMaster calorimetry metabolic analysis of one-year old
872 mice (SARAF-SIM1WT, n=10; SARAF-SIM1KO, n=6). **D**, Heat production over time, and heat
873 production per body weight (inset). **E**, Dark-phase locomotion. **F**, Total food intake. **G**, Inguinal
874 WAT, visceral WAT, liver and iBAT tissue histology in one-years-old SARAF-SIM1WT and

875 SARAF-SIM1KO mice. Size bar- 100µm. **H-I**, Inguinal, and visceral WAT droplet size
876 quantification. **J-K**, iBAT and liver pixels of fat droplets/area quantification.

877 **Figure 4: Hippocampal neurons proliferation, anxiety related behavioral phenotypes and**
878 **hepatocyte cellular phenotypes of SARAF$^{fl/fl}$PGK-Cre^{+} mice. A**, EDU(5-ethynyl-2′-
879 deoxyuridine) proliferation analysis of SARAF-WT and SARAF-KO mice at the dorsal and ventral
880 hippocampal dentate gyrus proliferation quantification. **B-C**, 3-month-old SARAF-WT (n=11)
881 and SARAF-KO (n=10) mice performance in anxiety-related tests: **B**, dark-light transfer. **C**,
882 Frequency of exits. **D**, Acoustic startle response test. Reaction time in 3 blocks of 120db stimuli.
883 **E**, Blood corticosterone levels following 15-minute restrain stress (SARAF-WT, n=8; SARAF-
884 KO, n=7). **F**, Fura-2AM Ca^{2+} imaging trace of primary hepatocytes extracted from SARAF-WT
885 and SARAF-KO mice and the quantification of SOCE levels (inset). **G**, Ca^{2+} oscillations in
886 hepatocytes induced by vasopressin (1nM) as measured by FURA-2AM. Quantification of Ca^{2+}
887 elevation and oscillation interval (inset). **H**, Mitochondrial respiration of SARAF-WT and
888 SARAF-KO primary hepatocytes and their spare respiratory capacity. **I**, Heatmap representation
889 of LXR/RXR hepatic (liver X receptor) pathway activation which was indicated by ingenuity
890 platform in MEF RNA sequencing results.

891 **Figure 1S: Characterization of SARAF-KO metabolic phenotype. A**, Western blot of the
892 whole-brain extracts from SARAF-WT, and SARAF-KO mice and from HEK293 cells (positive
893 control, PC). **B**, Linear growth measurement of one year-old mice (SARAF-WT, n=10; SARAF-
894 KO, n=6). **C**, food consumption 8 h refeed experiment, after 5 hours fasting during active phase
895 of three-months-old mice (SARAF-WT, n=7; SARAF-KO, n=9). **D**, Percentage of weight loss and
896 gain following refeed experiment of three-months old mice (SARAF-WT, n=7; SARAF-KO, n=9.
897 **E**, histological sections of inguinal and visceral WAT, iBAT and liver from three-month-old
898 SARAF-WT, and SARAF-KO mice. Size bar- 100µm. **F-I**, quantification sections as outlined in
899 E, Inguinal, and visceral WAT droplet size quantification and iBAT and liver pixels of fat
900 droplets/area quantification. **J**, Four-weeks voluntary wheel training effect over fold change of
901 lean/body weight and fat/body weight ratios. **K-M**, PhenoMaster calorimetry metabolic analysis
902 of one year-old mice after four-week voluntary wheel training. **K**, Heat production over time
903 (SARAF-WT, n=6; SARAF-KO, n=12). Insert AUC heat production. **L**, Dark-phase locomotion.
904 **M**, Total food intake.

905 **Figure 2S: Characterization of SARAF-SIM1KO metabolic phenotype. A**, Tissue punch PCR
906 validation of SARAF exon excision in the hypothalamus PVN, arrow indicates the product after
907 the removal of exon 3. **B**, Food consumed after five hours fasting at eight hours refeed experiment
908 in 1-years-old SARAF-SIM1WT and SARAF-SIM1KO mice. **C**, percentage of weight loss after
909 five hours fasting, and gain after eight hours refeed experiment in 1-years old SARAF-SIM1WT
910 (n=10) and SARAF-SIM1KO (n=6) mice. **D-F**, PhenoMaster calorimetry metabolic analysis of 3-
911 month-old SARAF-SIM1WT and SARAF-SIM1KO mice **D,** Heat production over time (SARAF-
912 SIM1WT, n=14; SARAF-SIM1KO, n=6). **E**, Dark-phase locomotion. **F**, Total food intake.

913 **Figure 3S: Metabolic phenotype of western diet fed SARAF-SIM1WT and SARAF-**
914 **SIM1KO. A**, mice body weight (SARAF-SIM1WT, n=5; SARAF-SIM1KO, n=11), **B**, Percent
915 lean mass change, and **C**, Percent change in body mass over a period of eighteen-weeks on western
916 diet. **D-E**, PhenoMaster calorimetry metabolic analysis during twelve weeks on western diet fed
917 mice. **D**, Heat production, **E**, Total food intake. **F**, Glucose tolerance test at twelve-weeks on
918 western diet. **G**, Inguinal and visceral WAT, BAT and liver H&E-stained tissue from mice after
919 eighteen weeks western on fed diet. **H-K** fat droplets/area quantification of the sections as shown
920 in G.

921 **Figure 4S: Characterization of SARAF-KO and SARAF-SIM1KO mice memory and**
922 **anxiety-related phenotypes. A**, Co-immunostaining of doublecortin (DCX) and β-gal and in
923 hippocampal section from *Saraf*$^{tm1a(KOMP)Wtsi}$ line. **B**, SARAF-WT and SARAF-KO ventral
924 hippocampal dentate gyrus proliferation quantification, number of PCNA positive cells out of
925 DCX positive cells. **C**, Assessment of proliferation using Ki67 in MEF cells. **D-E,** Y-maze assay
926 short memory test (SARAF-WT, n=11; SARAF-KO, n=10) and **F**, Morris Water Maze (MWM)
927 long-term memory assay of three-months old of SARAF-WT (n=7) and SARAF-KO (n=11) mice.
928 **G-H** DLT. G, Time in light. F. The frequency of Visits in lit section of three-months old SARAF-
929 SIM1WT and SARAF-SIM1KO mice. **I**, Acoustic startle response tests. Reaction time in 3 blocks
930 of 120db stimuli of three-month old SARAF-SIM1WT (n=14) and SARAF-SIM1KO (n=6) mice.

Fig. 1

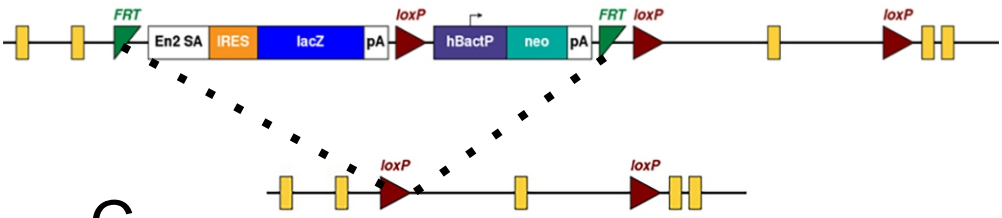
A
FRT
En2 SA
IRES
lacZ
pA
loxP
hBactP
neo
pA
FRT
loxP
loxP
loxP
loxP

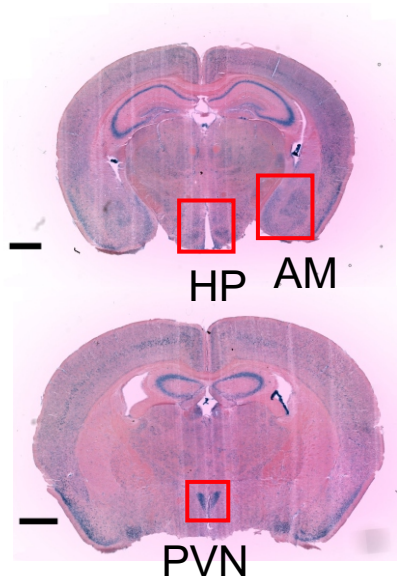
B
HP
AM
PVN

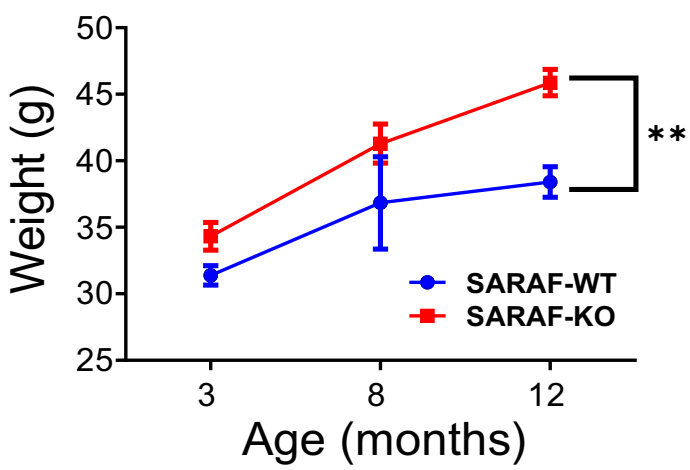
C
Weight (g)
50
45
40
35
30
25
3
8
12
Age (months)
SARAF-WT
SARAF-KO
**

KO
WT

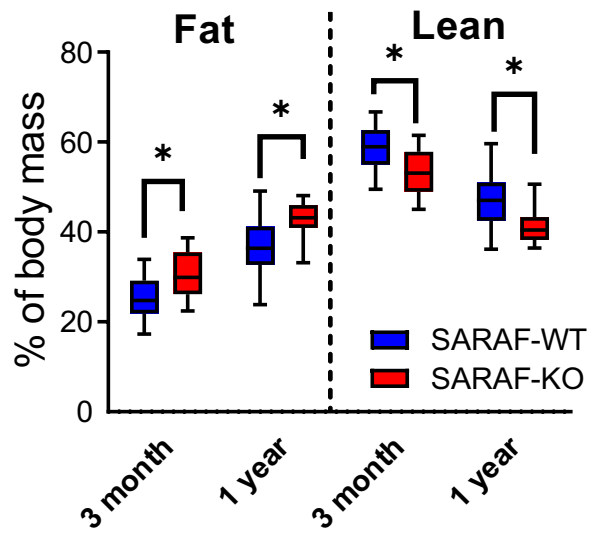
D
Fat
Lean
% of body mass
80
60
40
20
0
*
*
*
*
SARAF-WT
SARAF-KO
3 month
1 year
3 month
1 year

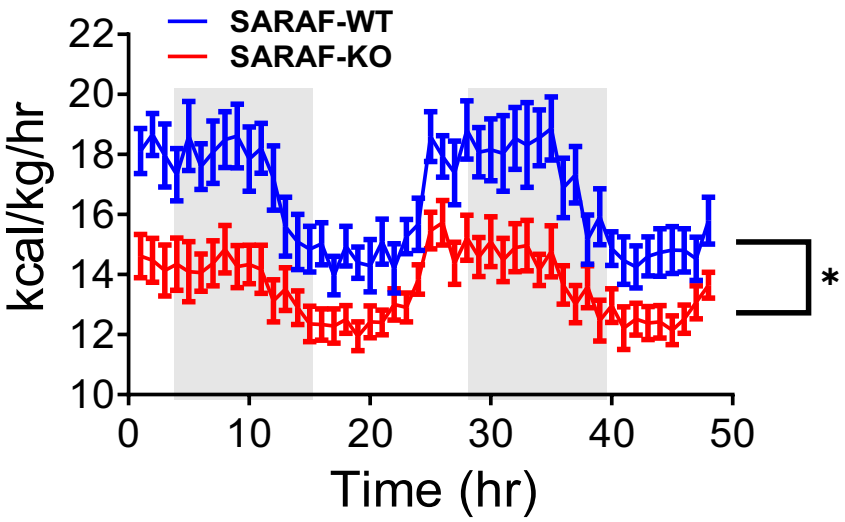
E
SARAF-WT
SARAF-KO
kcal/kg/hr
22
20
18
16
14
12
10
0
10
20
30
40
50
Time (hr)
*

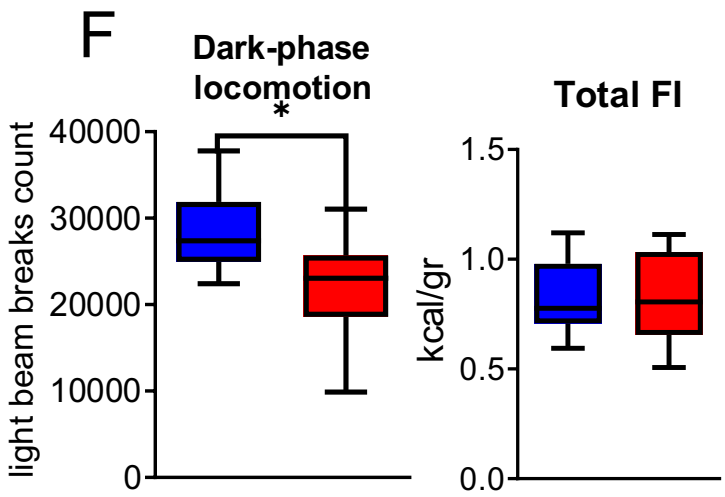
F
Dark-phase locomotion
*
light beam breaks count
40000
30000
20000
10000
0
Total FI
kcal/gr
1.5
1.0
0.5
0.0

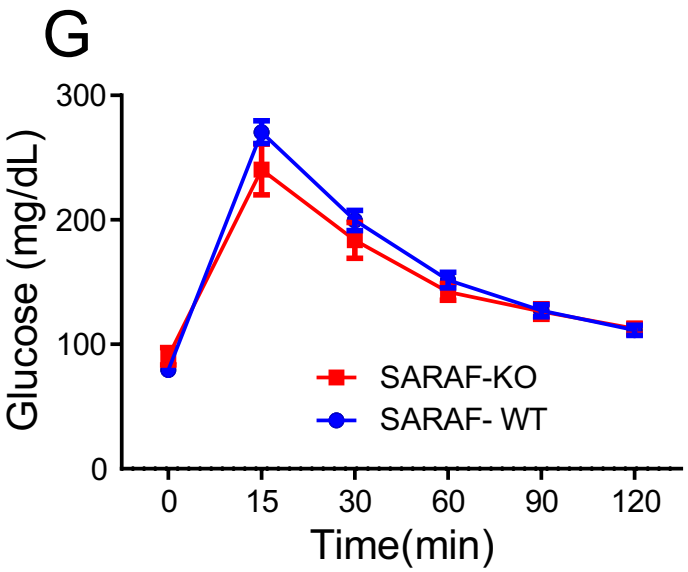
G
Glucose (mg/dL)
300
200
100
0
SARAF-KO
SARAF- WT
0
15
30
60
90
120
Time(min)

Fig. 2

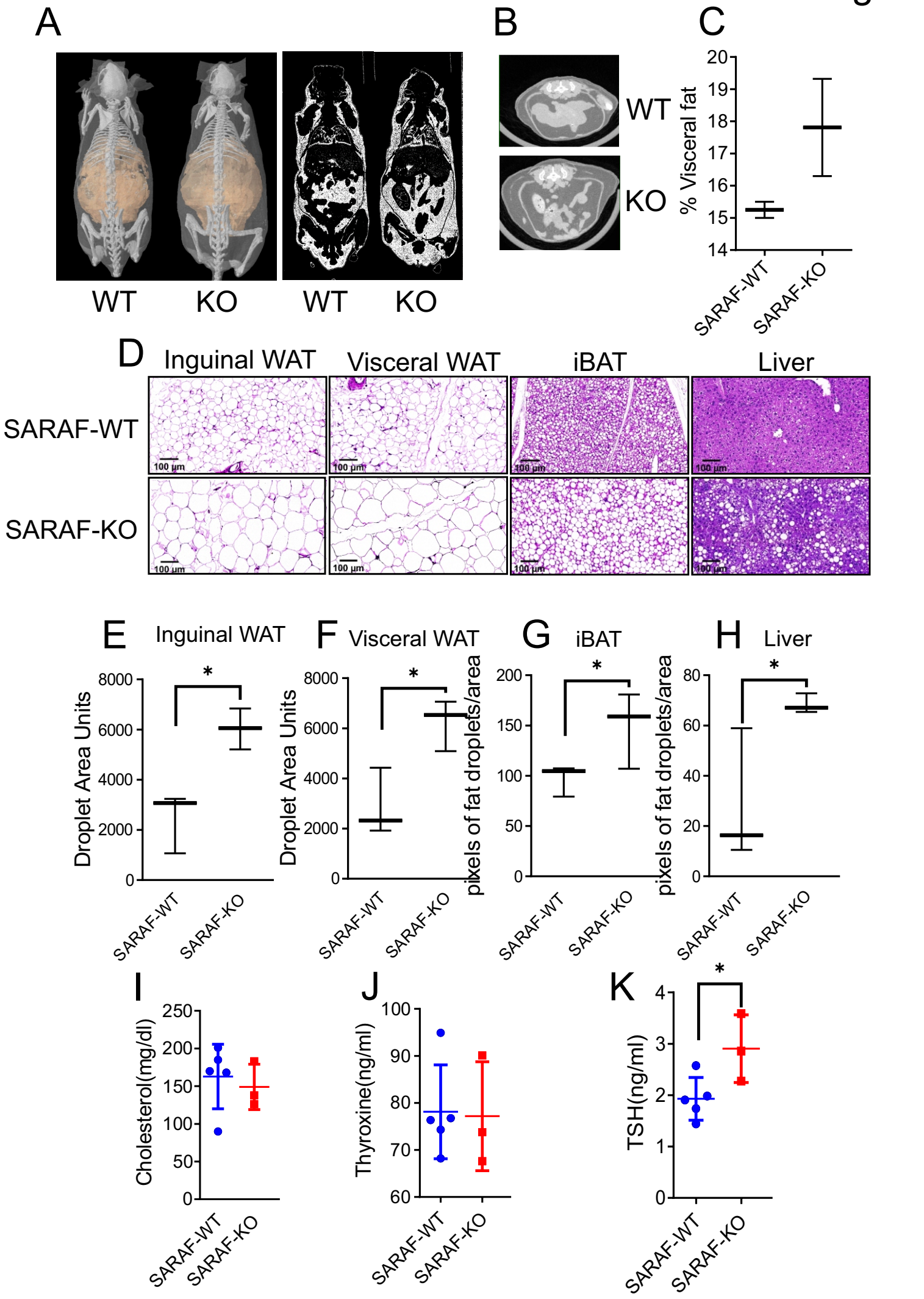
A
WT
KO
WT
KO
B
WT
KO
C
% Visceral fat
20
19
18
17
16
15
14
SARAF-WT
SARAF-KO
D
Inguinal WAT
Visceral WAT
iBAT
Liver
SARAF-WT
SARAF-KO
100 µm
E
Inguinal WAT
Droplet Area Units
8000
6000
4000
2000
0
*
SARAF-WT
SARAF-KO
F
Visceral WAT
Droplet Area Units
8000
6000
4000
2000
0
*
SARAF-WT
SARAF-KO
G
iBAT
pixels of fat droplets/area
200
150
100
50
0
*
SARAF-WT
SARAF-KO
H
Liver
pixels of fat droplets/area
80
60
40
20
0
*
SARAF-WT
SARAF-KO
I
Cholesterol(mg/dl)
250
200
150
100
50
0
SARAF-WT
SARAF-KO
J
Thyroxine(ng/ml)
100
90
80
70
60
SARAF-WT
SARAF-KO
K
TSH(ng/ml)
4
3
2
1
0
*
SARAF-WT
SARAF-KO

Fig. 3

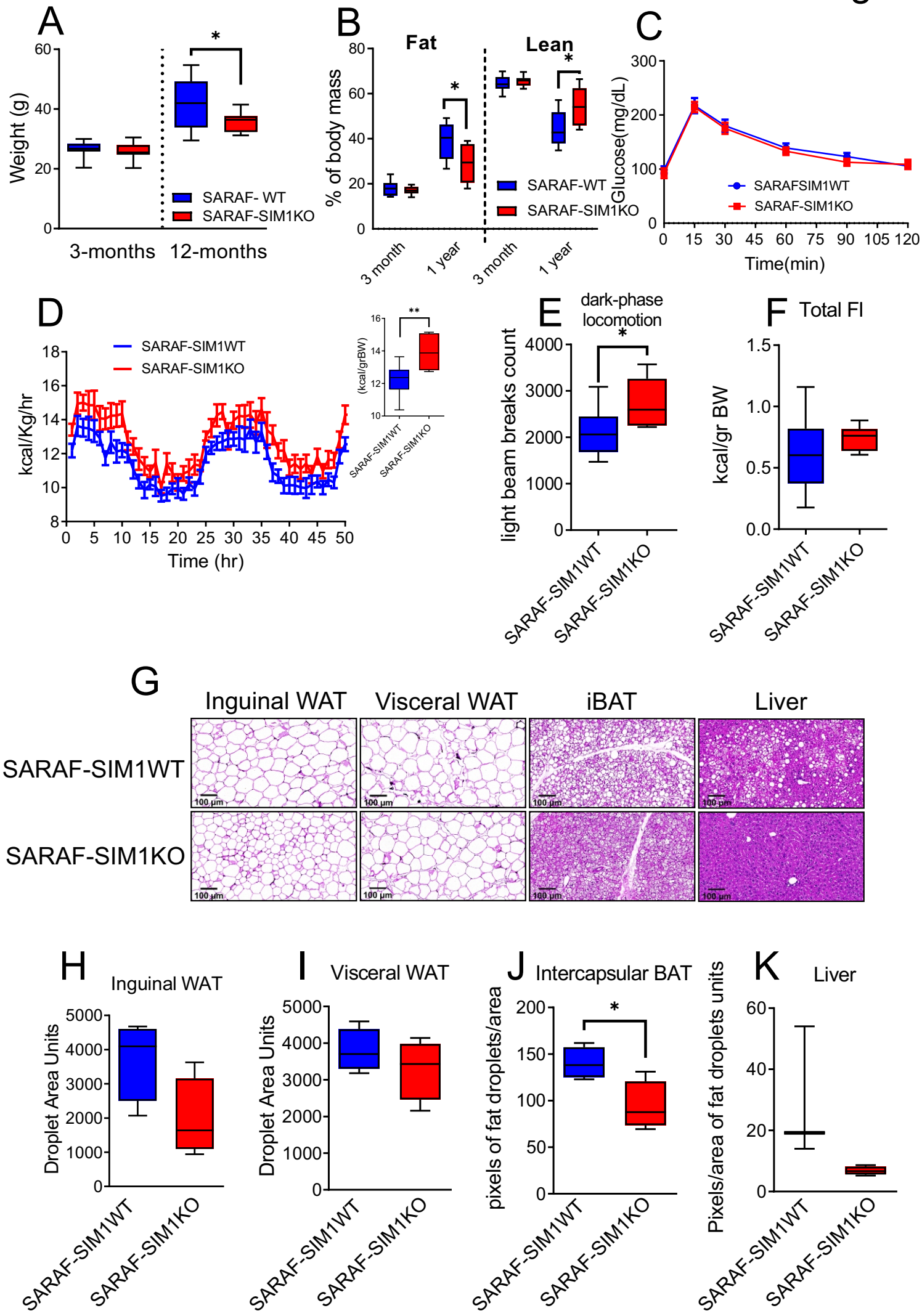
A
Weight (g)
SARAF- WT
SARAF-SIM1KO
3-months
12-months
B
Fat
Lean
% of body mass
SARAF-WT
SARAF-SIM1KO
3 month
1 year
C
Glucose(mg/dL)
SARAFSIM1WT
SARAF-SIM1KO
Time(min)
D
SARAF-SIM1WT
SARAF-SIM1KO
kcal/Kg/hr
Time (hr)
(kcal/grBW)
E
dark-phase locomotion
light beam breaks count
F
Total FI
kcal/gr BW
G
Inguinal WAT
Visceral WAT
iBAT
Liver
SARAF-SIM1WT
SARAF-SIM1KO
H
Inguinal WAT
Droplet Area Units
I
Visceral WAT
J
Intercapsular BAT
pixels of fat droplets/area
K
Liver
Pixels/area of fat droplets units

Fig. 4

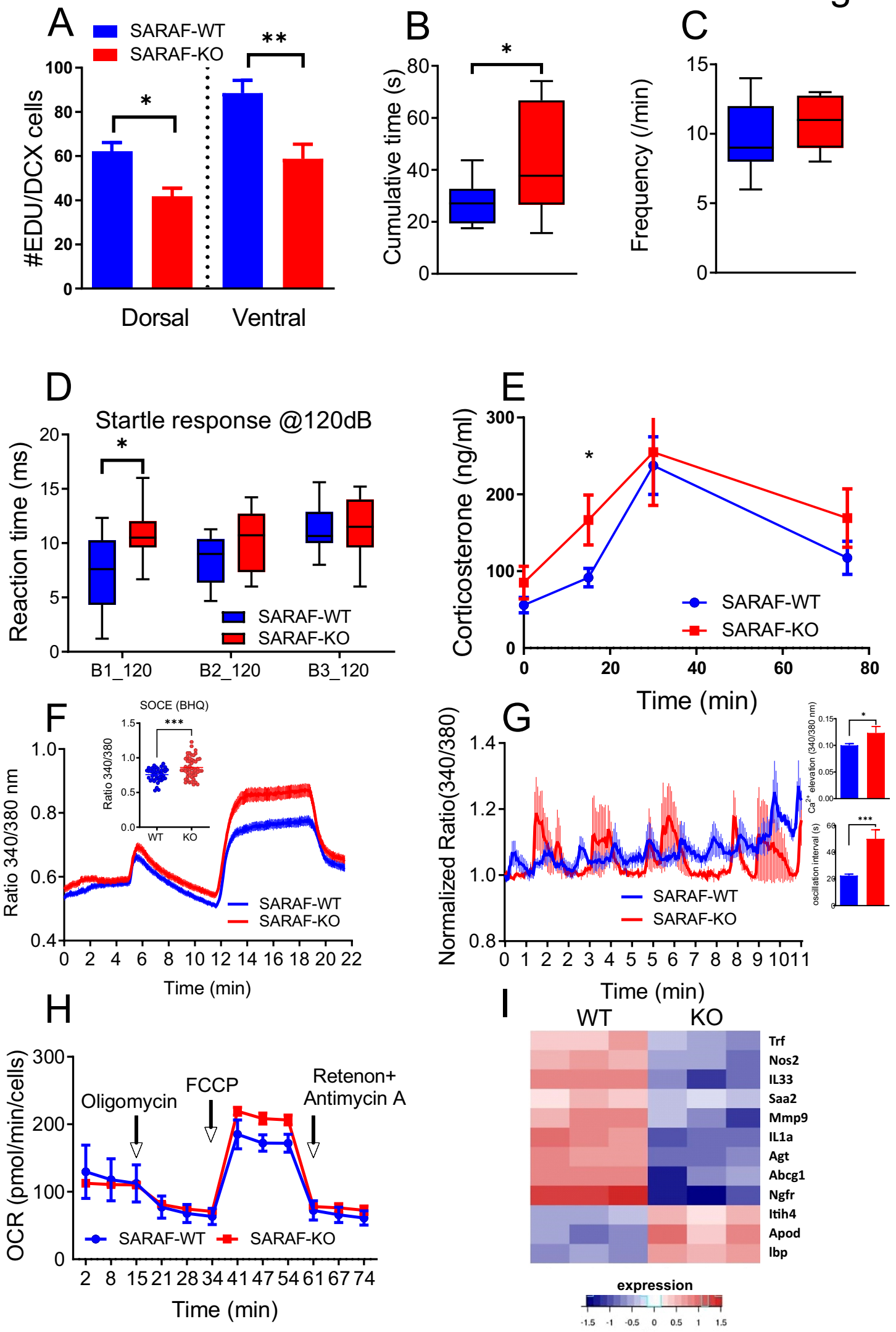
A
SARAF-WT
SARAF-KO
#EDU/DCX cells
Dorsal
Ventral
B
Cumulative time (s)
C
Frequency (/min)
D
Startle response @120dB
Reaction time (ms)
B1_120
B2_120
B3_120
E
Corticosterone (ng/ml)
Time (min)
F
SOCE (BHQ)
Ratio 340/380
WT
KO
Ratio 340/380 nm
Time (min)
G
Normalized Ratio(340/380)
Time (min)
H
Oligomycin
FCCP
Retenon+
Antimycin A
OCR (pmol/min/cells)
Time (min)
I
WT
KO
Trf
Nos2
IL33
Saa2
Mmp9
IL1a
Agt
Abcg1
Ngfr
Itih4
Apod
Ibp
expression

Fig. 1S

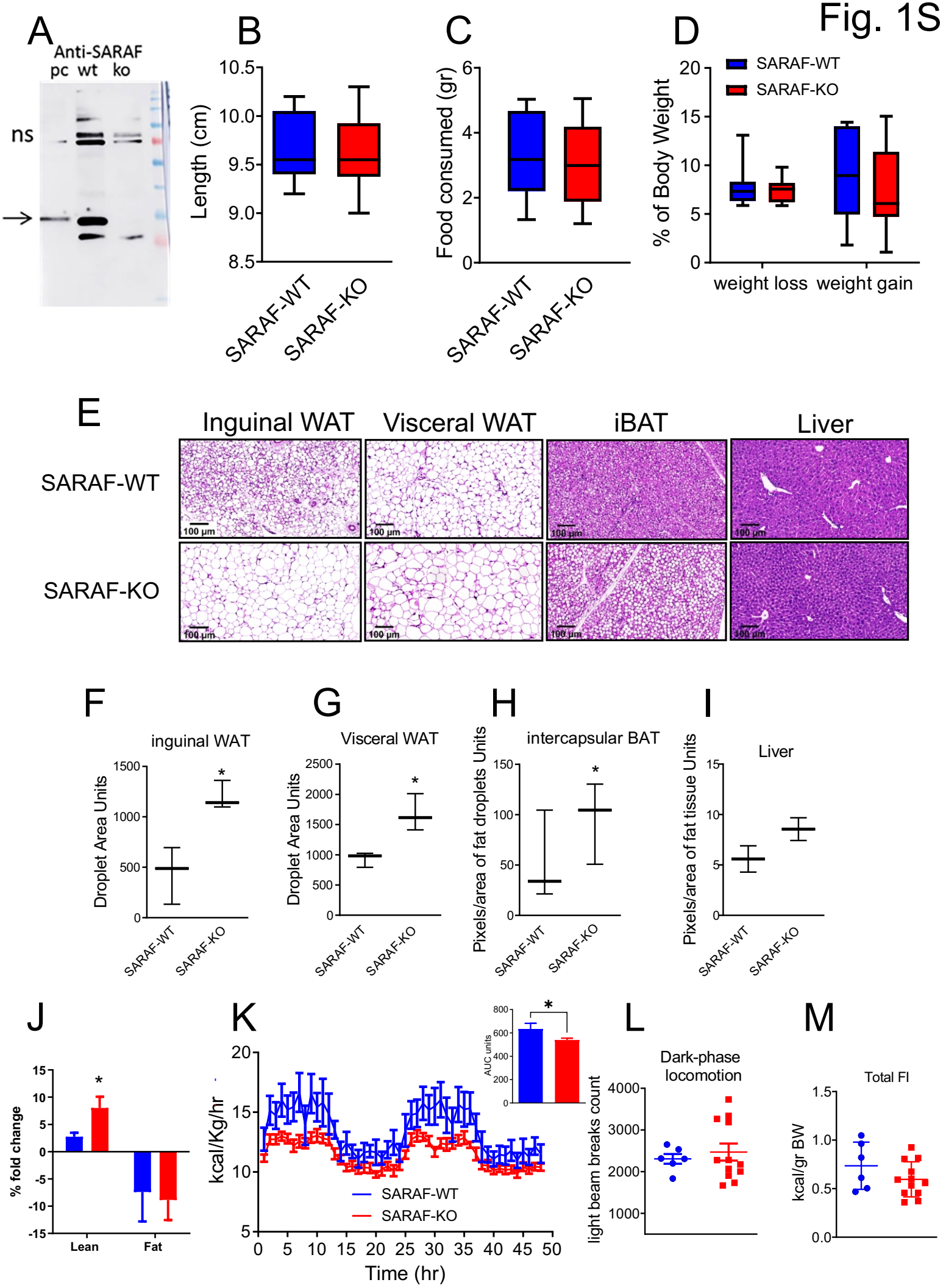
A
Anti-SARAF
pc wt ko
ns
B
Length (cm)
10.5
10.0
9.5
9.0
8.5
SARAF-WT
SARAF-KO
C
Food consumed (gr)
6
4
2
0
SARAF-WT
SARAF-KO
D
% of Body Weight
20
15
10
5
0
SARAF-WT
SARAF-KO
weight loss
weight gain
E
Inguinal WAT
Visceral WAT
iBAT
Liver
SARAF-WT
SARAF-KO
100 µm
F
inguinal WAT
Droplet Area Units
1500
1000
500
0
*
SARAF-WT
SARAF-KO
G
Visceral WAT
Droplet Area Units
2500
2000
1500
1000
500
0
*
SARAF-WT
SARAF-KO
H
intercapsular BAT
Pixels/area of fat droplets Units
150
100
50
0
*
SARAF-WT
SARAF-KO
I
Liver
Pixels/area of fat tissue Units
15
10
5
0
SARAF-WT
SARAF-KO
J
% fold change
15
10
5
0
-5
-10
-15
*
Lean
Fat
K
kcal/Kg/hr
20
15
10
5
0 5 10 15 20 25 30 35 40 45 50
Time (hr)
SARAF-WT
SARAF-KO
AUC units
800
600
400
200
0
*
L
Dark-phase locomotion
light beam breaks count
4000
3000
2000
1000
M
Total FI
kcal/gr BW
1.5
1.0
0.5
0.0

Fig. 2S

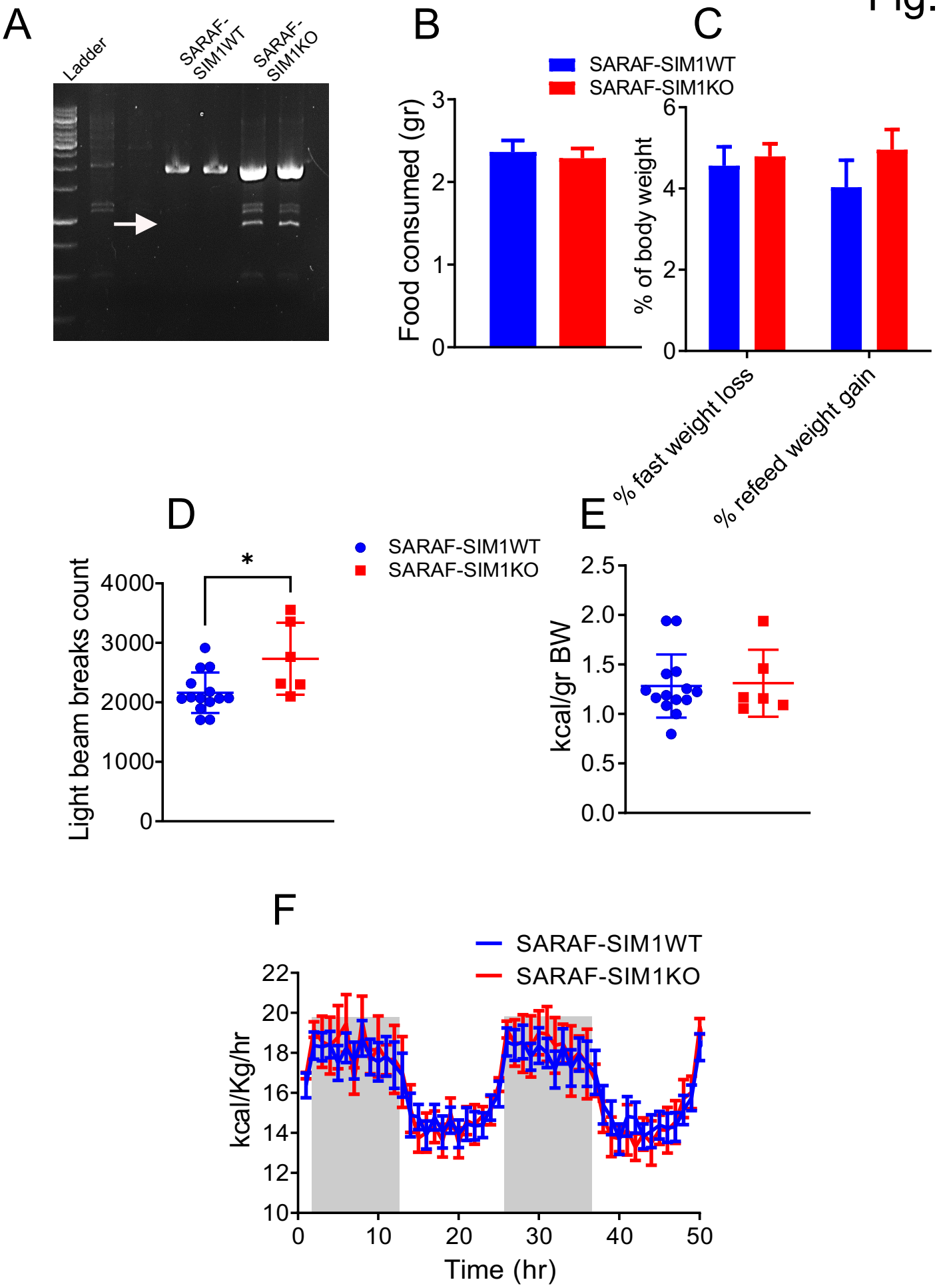
A
Ladder
SARAF-SIM1WT
SARAF-SIM1KO
B
Food consumed (gr)
0
1
2
3
C
SARAF-SIM1WT
SARAF-SIM1KO
% of body weight
0
2
4
6
% fast weight loss
% refeed weight gain
D
SARAF-SIM1WT
SARAF-SIM1KO
Light beam breaks count
0
1000
2000
3000
4000
*
E
kcal/gr BW
0.0
0.5
1.0
1.5
2.0
2.5
F
SARAF-SIM1WT
SARAF-SIM1KO
kcal/Kg/hr
10
12
14
16
18
20
22
0
10
20
30
40
50
Time (hr)

Fig. 3S

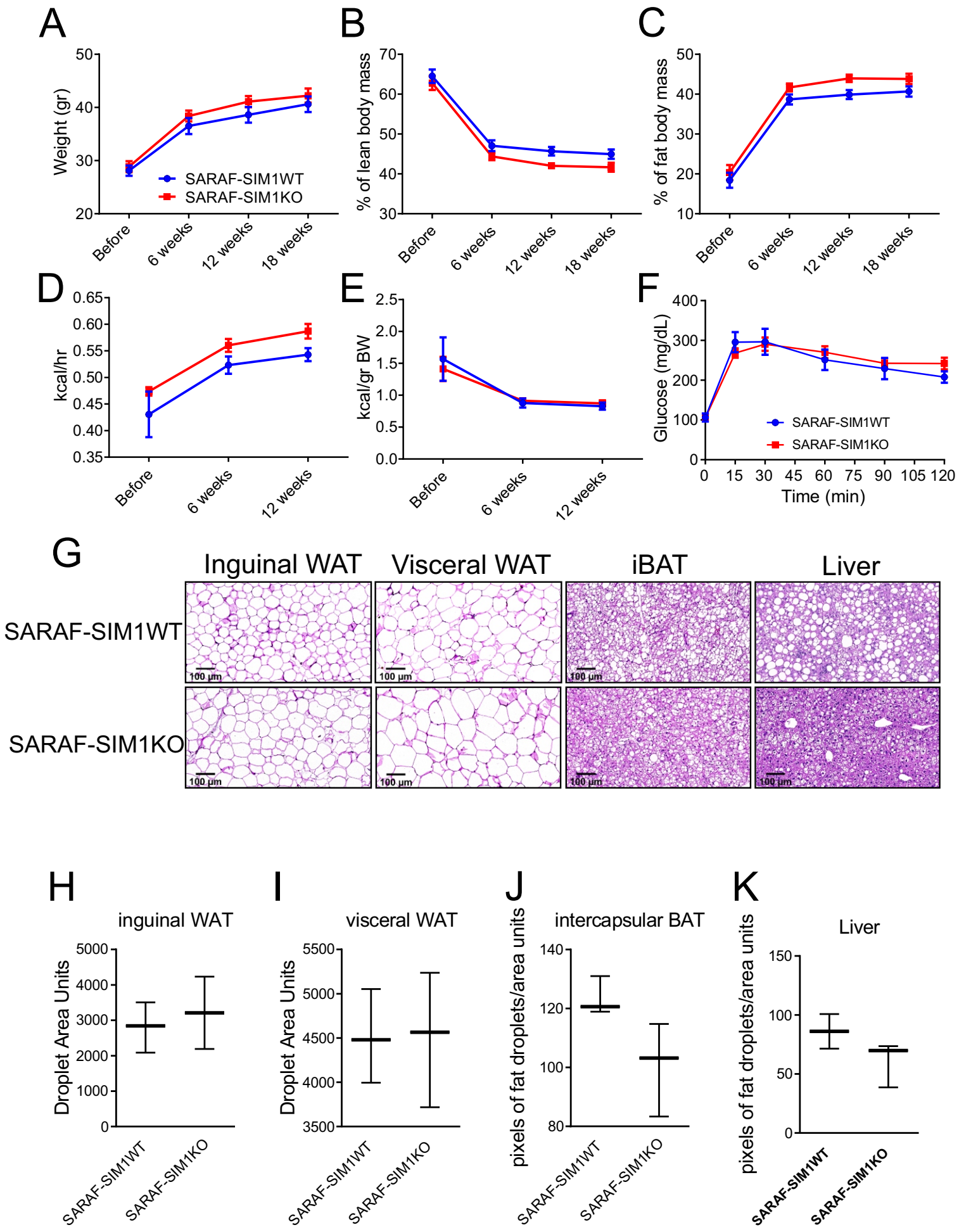
A
Weight (gr)
SARAF-SIM1WT
SARAF-SIM1KO
Before
6 weeks
12 weeks
18 weeks
B
% of lean body mass
C
% of fat body mass
D
kcal/hr
E
kcal/gr BW
F
Glucose (mg/dL)
Time (min)
G
Inguinal WAT
Visceral WAT
iBAT
Liver
SARAF-SIM1WT
SARAF-SIM1KO
100 µm
H
inguinal WAT
Droplet Area Units
I
visceral WAT
J
intercapsular BAT
pixels of fat droplets/area units
K
Liver

Fig. 4S

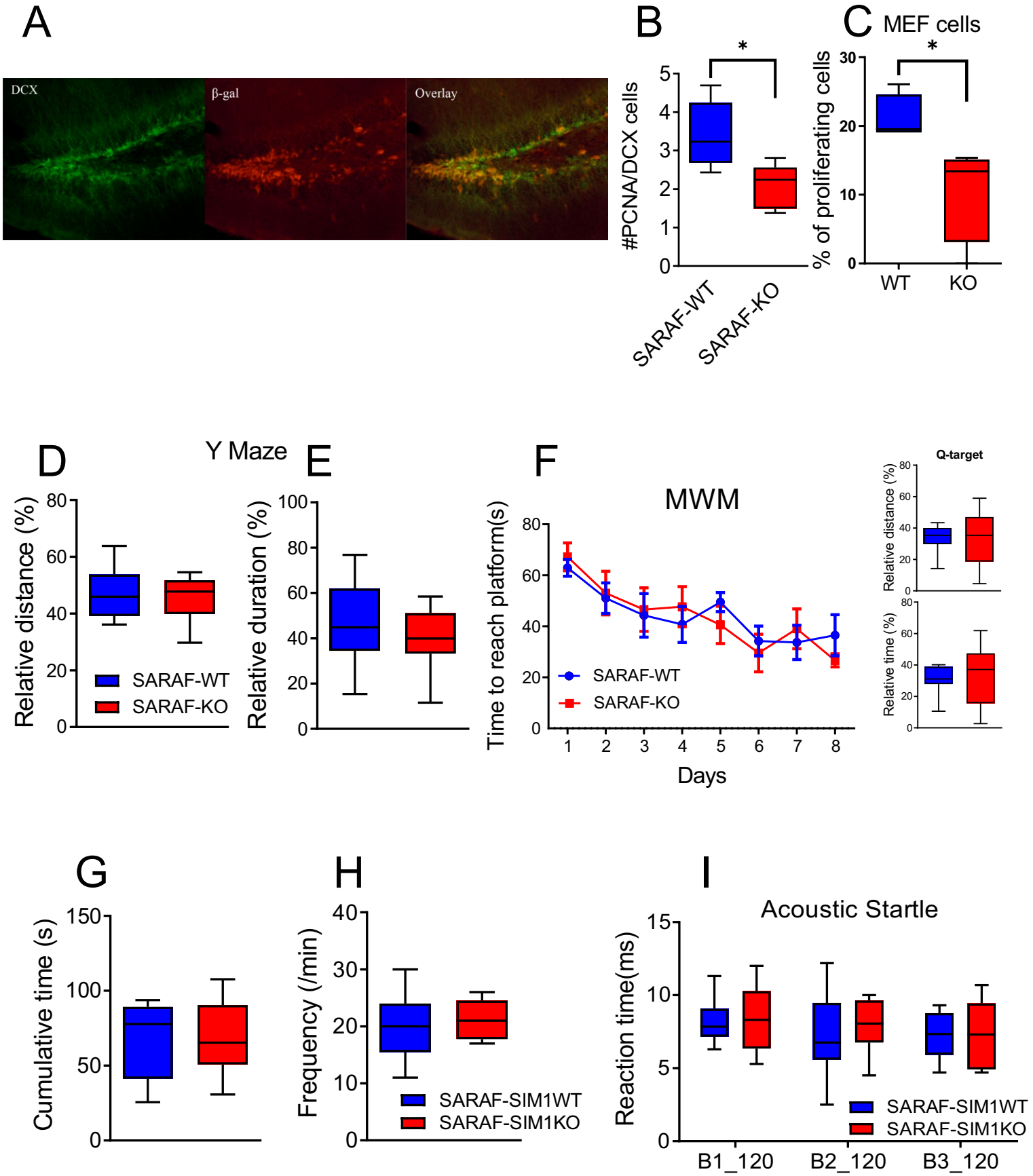
A
DCX
β-gal
Overlay
B
#PCNA/DCX cells
SARAF-WT
SARAF-KO
C MEF cells
% of proliferating cells
WT
KO
D
Y Maze
Relative distance (%)
SARAF-WT
SARAF-KO
E
Relative duration (%)
F
MWM
Time to reach platform(s)
Days
Q-target
Relative distance (%)
Relative time (%)
G
Cumulative time (s)
H
Frequency (/min)
SARAF-SIM1WT
SARAF-SIM1KO
I
Acoustic Startle
Reaction time(ms)
B1_120
B2_120
B3_120